February 2022
Report No. 22-025

Charles D. Baker
Governor
Karyn E. Polito
Lieutenant Governor
Jamey Tesler
MassDOT Secretary & CEO

Detecting Subsurface Voids in Roadways Using UAS with Infrared Thermal Imaging

Principal Investigator(s)
Dr. Alessandro
Dr. Tzuyang Yu
University of Massachusetts Lowell

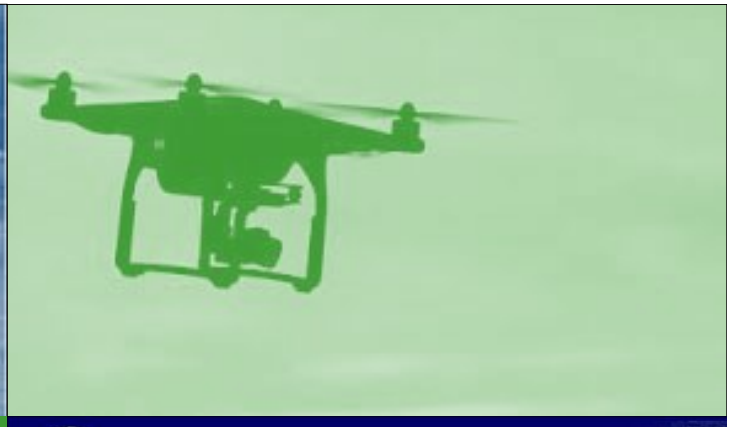

Research and Technology Transfer Section
MassDOT Office of Transportation Planning

U.S. Department of Transportation
Federal Highway Administration

Technical Report Document Page

1. Report No.	2. Government Accession No.	3. Recipient's Catalog No.
22-025		

4. Title and Subtitle	5. Report Date
Detecting Subsurface Voids in Roadways Using UAS with Infrared Thermal Imaging	February 2022
	6. Performing Organization Code

7. Authors	8. Performing Organization Report No.
Alessandro Sabato, Tzuyang Yu, Nitin Nagesh Kulkarni, and Shweta Dabetwar	22-025

9. Performing Organization Name and Address	10. Work Unit No. (TRAIS)
University of Massachusetts Lowell 600 Suffolk St., Lowell, MA 01854	11. Contract or Grant No. 112754

12. Sponsoring Agency Name and Address	13. Type of Report and Period Covered
Massachusetts Department of Transportation Office of Transportation Planning Ten Park Plaza, Suite 4150, Boston, MA 02116	Final Report February 2022 (November2022-February 2022)
	14. Sponsoring Agency Code n/a

15. Supplementary Notes
Project Champions - Jeff DeCarlo and Jason Benoit, MassDOT

16. Abstract
The failure of culverts and drainage piping underneath roadways creates sinkholes that represent a safety hazard to the traveling public and result in costly repairs and traffic inconveniences. The ability to detect voids before pavement collapse occurs is crucial for maintenance and replacement purposes. Routine inspections of culverts are hard to perform and require expensive and time-consuming techniques such as drain cameras or ground penetrating radar. This research validates a new method to detect roadway subsurface voids based on infrared (IR) imaging combined with unmanned aerial system surveying. Laboratory and field tests were necessary to develop mission-critical information that marked IR imaging's current performance and solved issues that characterized this technique. Advanced image post-processing techniques were also developed to improve the detection accuracy of IR imaging, showing that thermal photogrammetry can detect roadway subsurface voids that are representative of failing culverts and drainage pipes. This research developed a more accurate nondestructive evaluation approach for assessing the conditions of real-world underground structures that are crucial for their inspection, maintenance, and management.

17. Key Word	18. Distribution Statement
Nondestructive evaluation, infrared thermography, unmanned aerial system, culvert inspection, sinkholes.	

19. Security Classif. (of this report)	20. Security Classif. (of this page)	21. No. of Pages	22. Price
unclassified	unclassified	71	n/a

Form DOT F 1700.7 (8-72) Reproduction of completed page authorized

This page was left blank intentionally.

Detecting Subsurface Voids in Roadways Using UAS with Infrared Thermal Imaging

Final Report

Prepared By:

Dr. Alessandro Sabato
Principal Investigator

Dr. Tzuyang Yu
Co-Principal Investigator

Mr. Nitin Nagesh Kulkarni

Dr. Shweta Dabetwar

University of Massachusetts Lowell
600 Suffolk St., Lowell, MA 01854

Prepared For:

Massachusetts Department of Transportation
Office of Transportation Planning
Ten Park Plaza, Suite 4150
Boston, MA 02116

February 2022

This page was left blank intentionally.

Acknowledgments

Prepared in cooperation with the Massachusetts Department of Transportation, Office of Transportation Planning, and the United States Department of Transportation, Federal Highway Administration.

The project team would like to acknowledge the efforts of Mr. Jason Benoit, Dr. Jeffrey DeCarlo, Dr. Scott Uebelhart, Ms. Robin Grace, and Dr. Hongyan (Lily) Oliver for their support throughout the scope of the project. A special thanks to Jason Benoit for continuous support and helping with laboratory specimens procurement, test planning, outdoor testing, and technical feedback throughout the duration of the whole project.

Disclaimer

This page was left blank intentionally.

Executive Summary

This study of "Detecting Subsurface Voids in Roadways Using UAS with Infrared Thermal Imaging" was undertaken as part of the Massachusetts Department of Transportation (MassDOT) Research Program. This program is funded with Federal Highway Administration (FHWA) State Planning and Research (SPR) funds. Through this program, applied research is conducted on topics of importance to the Commonwealth of Massachusetts transportation agencies.

The opening of soil voids underneath roadway pavement caused by the failure of underground structures such as culverts and drainage piping create a safety hazard to the traveling public. Water infiltration and soil erosion initiated by damaged or collapsed culverts may create sinkholes that result in costly repairs and traffic inconveniences. The cost of a culvert repair ranges from a few thousand dollars to $32,000, and costs can be even higher if the culvert failure causes the roadway to collapse. Knowledge about the location, severity, and depth of soil voids above underground structures can be used as an alert system and is crucial for roadways preservation projects, plan effective maintenance, and system repair.

Because of the large number of culverts, many of which are located in remote areas or are subjected to high-volume traffic, routine inspections are hard to achieve. Currently, inspecting culverts and other underground structures requires expensive or time-consuming techniques such as laser scan inspection, drain cameras, or ground penetrating radar (GPR). While laser scanners and drain cameras require direct access to the culvert from the side of the road through streams or drainage channels, GPR uses electromagnetic pulses (EMPs) to image the culvert from the road's surface using the reflected signals. However, results of GPR analyses are challenging to interpret by untrained personnel and are affected by dielectric conduction losses, uncertainty about the composition of the inspected material, and signal scattering due to material inhomogeneity. As a result, MassDOT personnel remarked on the lack of proper tools to identify the location of drainage pipelines and the quantity of filling material used to repair sinkholes. Thus, nondestructive approaches that are more accurate and cost-effective and capable of eliminating traffic congestion and risk for the inspectors are sought and motivated this research.

Novel advancements in computer vision and image processing techniques have made infrared thermography (IRT) a powerful method to assess the conditions of large-scale systems and create heat maps of physical attributes. IRT has shown capabilities in detecting subsurface defects in various engineering structures and materials, especially when combined with unmanned aerial systems (UASs). In early 2020, MassDOT's divisions of Highway and Aeronautics performed some pilot tests to study the feasibility of UAS-borne IRT inspection of roadways to identify drainage pipes and culverts from thermal images. However, results were inconclusive and inaccurate, and methodic characterization of the infrared (IR) imaging's capability to be a more cost-effective method for rapid large-scale transportation infrastructure inspection and subsurface damage evaluation was still missing. For these reasons, laboratory and field tests were necessary to develop mission-critical information to mark IR imaging's performance and solve issues that still characterize this technique. Mission-specific variables

such as the correlation between visible and IR spectrum images, IR images resolution and accuracy, UAS motion, shadow effects, thermal warming related to vehicle tire traffic, and weather conditions needed to be considered before field deployment.

The research leveraged UASs to improve the efficiency and flexibility of IRT in detecting voids above damaged culverts and drainage pipes. More specifically, this research focuses on the experimental validation of rapid aerial infrared thermography (AIR_T) and UASs for (i) detecting soil voids and (ii) quantifying the dimension and severity of those defects before they fail in service of the affected infrastructure. The specific goals of this research included the following:

- Develop post-processing algorithms for image de-noising and correction to improve the detection accuracy of IRT;
- Determine the accuracy of IR systems as a function of depth and for field inspections to detect soil voids; and
- Define operational problems associated with its field deployment and suggest operating procedures to optimize the use of IR imaging on UAS platforms.

To validate the accuracy of the proposed UAS-AIR_T, laboratory and field tests were performed. The former was conducted on a lab-scale mock roadway based on MassDOT's standards for highways, roadways, and pavements to validate the accuracy of IRT in a controlled environment. During those tests, the smallest defect size detectable with IRT was investigated and compared with GPR-based results. In addition, the accuracy of the IRT method as a function of (i) camera distance, (ii) camera tilt angle, (iii) defect depth, (iv) moisture content, and (v) temperature difference was investigated. Field tests were performed to validate the UAS-AIR_T tool and define new inspection processes and protocols. A UAS embedding a high-resolution IR camera was used to inspect damaged and undamaged portions of roadways on top of culverts, overlay IR with digital images, and locate positions of defects. The undamaged portion of a roadway was used as a baseline and compared with damaged cases to identify the thermal signatures of defects and fill materials.

Because IRT suffers from poor signal-to-noise ratio (SNR), three different image post-processing algorithms were refined to improve the accuracy of the technique and locate the subsurface voids caused by a failing culvert: (i) R^2-based damage analysis, (ii) principal component thermography (PCT), and (iii) sparse-principal component thermography (S-PCT). The three approaches were quantified as a function of the image sampling rate used to collect data (i.e., the time interval between two subsequent IR photos) and the size of the defect. The tests proved that PCT and S-PCT were effective approaches to enhance the possibility of detecting subsurface voids. S-PCT can quantify the dimension of the subsurface voids with an error below 5% when proper sampling parameters are selected.

To finish, this report contains a section in which best practices and lessons learned are described. The section includes the procedures for operating the UAS in a real-world environment (e.g., time of the inspection, working distance, specific IR methods) to minimize the risk of false positive and increase the damage detection accuracy.

Table of Contents

This page was left blank intentionally

List of Tables

List of Figures

List of Acronyms

Acronym	Expansion
AIR_T	Aerial Infrared Thermography
COD	Coefficient of Determination
DVS	Downward Vision System
EI	Electromagnetic Induction
EM	Electromagnetic
EOF	Empirical Orthogonal Function
FAA	Federal Aviation Administration
FOV	Field of View
GPR	Ground Penetrating Radar
GSD	Ground Sampling Distance
IR	Infrared
IRT	Infrared Thermography
MassDOT	Massachusetts Department of Transportation
MT	Modulated Thermography
NDE	Nondestructive Evaluation
PCA	Principal Component Analysis
PCT	Principal Component Thermography
PPT	Pulse-phase Thermography
PT	Pulsed Thermography
RPC	Remote Pilot in Command
RWIS	Road Weather Information System
SHM	Structural Health Monitoring
SNR	Signal-to-Noise Ratio
S-PCT	Sparse-Principal Component Thermography
SVD	Singular Value Decomposition
SURF	Speeded Up Robust Feature
UAS	Unmanned Aerial System

This page was left blank intentionally.

1.0 Introduction

This study of "Detecting Subsurface Voids in Roadways Using UAS with Infrared Thermal Imaging" was undertaken as part of the Massachusetts Department of Transportation (MassDOT) Research Program. This program is funded with Federal Highway Administration (FHWA) State Planning and Research (SPR) funds. Through this program, applied research is conducted on topics of importance to the Commonwealth of Massachusetts transportation agencies.

Culverts and drainage pipes are used as the drainage, sewer, or water channels that run under a road. Damages in a culvert facilitate soil erosion and material loss from the road subgrade, creating voids underneath the pavement *(1)*. As erosion continues, the subsurface void size increases, resulting in sinkholes and the failure of the unsupported pavement if not repaired in time *(2,3)*. Sinkholes caused by small underground cavities and subsurface voids that expand over time resulted in safety hazards, traffic inconveniences, and expensive repairs in the United States. For example, in 2008, a culvert on Interstate 25 in Denver, Colorado, collapsed and created a two-lane-wide sinkhole that caused road shutdown and delays. The final repair of the 90-foot long culvert took several days and cost ~$1 million. The poor and mediocre conditions of 43% of North America's roadways, combined with the increase in severe weather events, accelerate the degradation process of the infrastructure *(4)*. Based on the severity of the damages, repair actions range from retrofitting to trenching a new pipeline. A cost analysis performed by the Minnesota DOT on 550 repaired culverts reported costs ranging from $1,000 to $32,000 per rehabilitation project *(5)*. Structural assessment and retrofitting before failures in service can help save a significant amount of money, labor, and inconvenience for the traveling public. For these reasons, cost-effective monitoring approaches must be developed to keep up with maintenance needs without interrupting the roadways' everyday operations and affecting the economy.

While it is crucial to determine damages early in their life cycles, detecting subsurface voids in roadways caused by failing underground structures is a complex problem that requires labor, time, and extensive capital. Culverts are located in remote areas or underneath roadways characterized by high-volume traffic, making routine inspections and maintenance challenging tasks. DOT personnel laments a lack of proper tools to assess the conditions of culverts because currently used methods are inaccurate and difficult to deploy in real-world scenarios. A precise, cost-effective, and quick method for large-scale inspection and subsurface damage evaluation is missing.

In this study, the feasibility of using infrared (IR) imaging combined with UASs is investigated as nondestructive evaluation (NDE) techniques for culverts and drainage pipes. This research aims to determine the capability of IRT to detect roadway subsurface voids at an early stage while reducing traffic congestion and risks for the inspectors. In particular, the research focuses on the experimental validation of rapid aerial IRT (AIR_T) and UAS for (i) detecting soil voids and (ii) quantifying the dimension and severity of those defects before they result in failure-in-service of the roadway. Because an accurate and methodic characterization of the IRT's capability to be a more cost-effective method for inspection and subsurface damage evaluation

is missing, this study provides elements to improve the decision-making process of highway maintenance engineers and the possibility to access more accurate information about the location and severity of damages in roadways. MassDOT personnel is provided with a promising system to monitor in-service roadways to extend their operational life while reducing traffic congestion and risks for the inspection engineers.

This report is organized as follows: the rest of the introduction summarizes currently used culvert inspection methods, the operational principles of IRT and its applications, and the use of UASs for civil engineering infrastructure monitoring. Section 2 (Research Methodology) describes the laboratory and field tests used to validate the proposed approach, followed by a discussion about the analytical framework developed to post-process the IR images and detect subsurface voids. The outcomes of the experiments performed on a lab-scale roadway and the findings of the outdoor tests carried out on three culverts using a UAS to mount an IR camera are presented in Section 3 (Results). Lessons learned and conclusions are drawn in Section 4 (Best Practices and Conclusions).

1.1 Currently Used Inspection Techniques for Culvert Assessment

Multiple technologies have been developed for roadways monitoring and subsurface voids detection. These include alternating current (AC) resistivity, electromagnetic induction (EI), seismic reflection and refraction, and GPR, with each of them having advantages and disadvantages *(6–12)*. GPR is the most widely used approach for roadway inspection *(13)*. GPR is a nondestructive evaluation (NDE) technique in which an electromagnetic (EM) wave in the 10 MHz to 2.6 GHz range is transmitted through the soil, and its reflection is used to image any subsurface discontinuity. In the presence of a subsurface defect, the backscattered signal changes and that modification can be used for gathering information about the depth and severity of the damage *(14,15)*. Several advancements are currently taking place in GPR technologies that focus on signal post-processing *(16–18)*. However, GPR analyses are complicated to be interpreted by untrained personnel because of dielectric conduction losses, uncertainty about the composition of the inspected material, and signal scattering due to inhomogeneity. GPR tends not to be very accurate for practical applications due to different materials and layers of thickness of the roadways *(19,20)*. Despite the significant effort to improve GPR systems in recent years, this method is still not robust and accurate enough to locate subsurface defects in roadways caused by failing culverts. In addition, GPR is a very time-consuming and expensive technique and very difficult to be used for large-scale inspections. For example, using GPR on high-traffic-volume roads is challenging, making this technology unsuitable in densely populated regions without blocking the roadways for long periods.

In recent years, specialized robots embedding cameras have been designed for culvert assessment *(21)*. Based on the specific inspection goals, different cameras or sensing techniques are used. For example, end-to-end pipe inspections are carried out by mounting a camera with flashlights to collect videos and images from the inside of the culvert to spot defects, holes, and signs of corrosion *(22)*. Other approaches rely on using a laser scanner

mounted on the robot to recreate a three-dimensional point cloud of the inside of the structure and assess its conditions *(23)*. An attempt to use IRT by using a robot installing an IR camera and halogen lights to heat the culvert has been proposed too. However, this approach proved feasible only for culverts with a diameter larger than 1.2 m (47.2 in.) *(24)*.

1.2 Infrared Thermography for Condition Monitoring

Among many available techniques, IRT offers the possibility to examine and monitor aging structures efficiently. The basic principle behind IRT inspection is that subsurface defects modify the heat flow through the material. Voids or structural discontinuities in the object being inspected cause a variation in temperature of the material surface, which a thermal camera can capture. The thermal camera measures the heat transfer mechanism between the object being tested and the environment by detecting the IR radiation emitted by the object. Specifically, any surface with a temperature higher than the absolute zero (i.e., 0°K) emits energy in the form of electromagnetic (EM) radiation as a function of its temperature according to the Stefan–Boltzmann law. As shown in Figure 1.1, the emission of IR radiation occurs with EM waves having a wavelength in the 0.75–12 μm range. The radiation can be converted to temperature values through the material's emissivity (i.e., effectiveness in emitting energy as thermal radiation). Since IR radiations are not visible to the human eye, tailored sensors called bolometers are needed to detect the emitted wavelengths *(25)*.

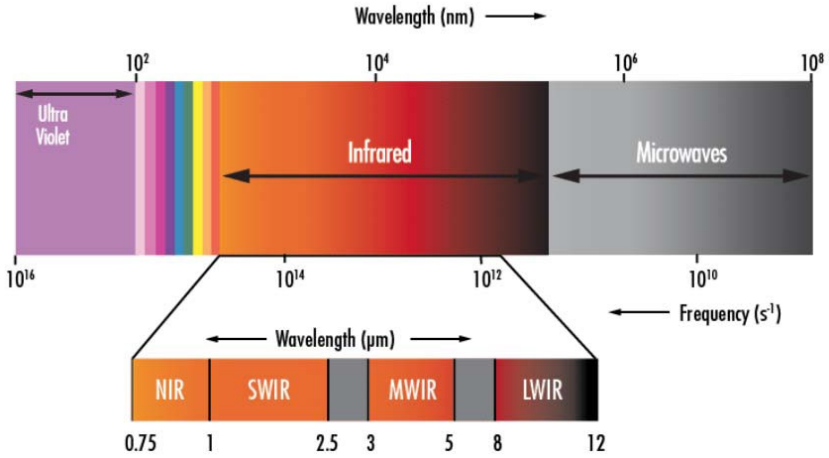

Figure 1.1: Electromagnetic spectrum with infrared region

To generalize, abnormal temperature profiles in the IR images indicate potential defects. Damages in the structure can be highlighted by local variations in the uniformity of the surface temperature. Because the thermal conductivity of air is lower than that of soil and asphalt, a thermal gradient is caused by voids that can be recorded with an IR camera. The heat flow between the lower and upper layers of the pavement depends on the temperature difference. The heat flow changes as soon as an area characterized by cracks, voids, or water infiltration

is present in the material's structure. This process is shown in Figure 1.2 for a concrete slab that absorbs heat during the day and releases it at night *(26)*. During the day, when the sun and air temperature are heating the material, areas above a subsurface defect warmth faster than those where the concrete is intact. For this reason, during the day, voids and delamination defects can be detected as warmer spots compared to undamaged parts. On the contrary, the thermal behavior is inverted during the night. The temperature of the structure decreases and surfaces above a void cool down faster compared to undamaged areas. As a result, the defect appears as a cold spot. Generally, defects are detected by a qualitative assessment of IR images as areas in the image having a high thermal contrast (i.e., hot or cold spots) compared to undamaged areas *(27–29)*. The intensity of the thermal contrast for a subsurface anomaly varies with its depth so that a void near the surface would create a more significant contrast than deeper defects. Figure 1.2 shows thermal radiation emitted from an object and how it is used to find subsurface defects *(30)*.

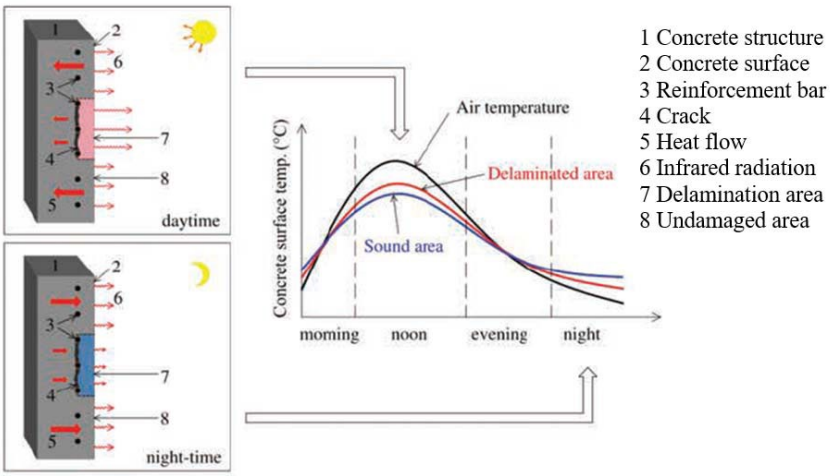

Figure 1.2: Thermal radiation emitted from object

Based on the excitation method used to warm the structure, IRT is classified as flash or pulsed thermography (PT), modulated thermography (MT), and pulse-phase thermography (PPT) *(31)*. In PT, the specimen is warmed up with a heat flash/pulse before collecting the images *(32)*. In MT, a sinusoidal temperature excitation is used before recording the data. The modulated frequency used for the thermal excitation is case-specific to improve results accuracy. In PPT, PT and MT are used simultaneously. First, the object is pulse heated; then it is exposed to a thermal excitation that is frequency modulated *(33)*. IRT is also categorized as active or passive. The former is based on external excitation methods for creating a temperature difference. In contrast, external excitation is not required in passive thermography and the detection is based on the energy emitted by the object naturally *(34)*. Although active thermography allows better defect detection by increasing the temperature difference between the test object and the environment, the possibility of having outliers in the results is higher than the passive method. In large-scale applications such as bridges and building inspections, warming up the structure before the test is not practical due to the size of the inspected areas *(35)*. Therefore the thermal excitation of the sun is used, and the inspection is performed when external environmental conditions guarantee the most significant temperature difference.

Therefore, passive IRT is performed at dusk or at night after the structure has been heated by the sun during the day *(30*, *37)*.

The use of IRT for structural health monitoring (SHM) and NDE has increased significantly in recent years, mainly because of cheaper IR cameras and advanced detection algorithms *(38*, *39)*. Traditionally, IRT has been used primarily for energy audit *(40–44)*, material characterization *(45–48)*, and only recently for SHM of civil structures *(49*, *50)*. IRT has transitioned from being used as a laboratory technique to a tool to detect subsurface defects for large-scale systems and civil engineering infrastructure in real-world scenarios *(51–53)*. IRT has been used for remote, rapid, and accurate imaging of concrete structures *(54)*. Because of their strategic relevance, bridges have been among the main applications of IRT in the civil engineering domain *(30*, *35)*. For example, IRT has been used to detect air trapped in bridge decks representing voids in the concrete structure *(55–57)*. Other studies developed automated procedures for detecting and classifying delamination in concrete bridge decks *(58)* and corrosion in steel bridges using deep learning *(59)*. Even if in smaller numbers compared to the bridge-related applications, IRT has been used to inspect dams and evaluate defects in their structure *(60)*, roadways *(61)*, leaks in underground pipelines *(62)*, and culverts *(63)*. It is interesting noticing that the approach proposed in *(63)* resembles the one of this research. However, that study is based on a laboratory validation only and the roadway is a metallic slab that is not representative of real-world conditions.

1.3 Applications of Unmanned Aerial Systems for Civil Structures Health Monitoring

NDE techniques based on computer vision have gained popularity in recent years because of their non-contact nature that simplifies the inspection of large areas *(64)*. In addition, when computer vision methods are paired with UASs, the image acquisition process is expedited and made more flexible. Combinations of photogrammetry and UAS have been used for the inspection of bridges *(65*, *66)*, dams *(67)*, and SHM of aging structures *(68)*. UASs were also used to measure truss members and reconstruct 3D models of the structure to detect damages *(69)* and track deformation and surface changes by analyzing the generated point clouds *(70)*.

The use of UASs can also help to inspect areas that are difficult to access or hazardous. In many cases, traditional inspections are not only dangerous but also impossible. In situations like these, the application of UASs for the inspection of large-scale systems has been a promising approach *(71)*. Videos collected using UASs have been used to measure structural deformations in a building caused by earthquakes and assess structural reliability *(72)*. Another application of UAS-based videography focused on determining the location and size of cracks in concrete beams, which can be expanded to inspect damages in civil infrastructure *(73)*. As observed, UAS-based inspection technologies can be combined with image processing methods to detect small cracks by combining the benefits of remote inspections with high precision measurement for areas difficult to reach *(74)*.

Applications of UAS for inspection have also gained popularity because of the possibility of performing SHM/NDE assessment and limiting interference with the targeted objects. Researchers proved that IRT inspections of bridges could be done using IR cameras installed on vehicles moving at driving speed *(75)* and on UASs *(76)* to reduce interference with traffic and limit lanes closure. Hence, it can be seen that recent advancements in drone-based technologies have made the SHM of civil infrastructure even more efficient.

2.0 Research Methodology

In early 2020, the MassDOT Highway and Aeronautics Divisions performed pilot tests to study the feasibility of UAS-borne IR inspection of roadways to identify drainage pipes and culverts from thermal images. The results of the pilot tests suggested some ability to identify damages in those systems. However, the outcomes of the study were inconclusive with regard to the accuracy or performance of IRT. An accurate and methodic characterization of the IR imaging's capability to be a more cost-effective method for rapid large-scale transportation infrastructure inspection and subsurface damage evaluation is still missing, which justifies the scope of this work. The research relies on an experimental validation for quantifying the efficiency of the proposed UAS-AIR_T system for (i) detecting soil voids and (ii) quantifying the dimension and severity of those defects before they cause failure-in-service of the affected infrastructure. This study aims to develop mission-critical information that can mark IR imaging's performance and solve issues that still characterize this technique through laboratory experiments and field tests. The specific goals of this research include the following:

- Determine the accuracy of IR systems as a function of defects depth and severity,
- Develop post-processing algorithms for image de-noising and correction to improve the detection accuracy of IRT, and
- Define operational problems associated with the field deployment of the technology and suggest operating procedures to optimize the use of IRT on UAS platforms.

This section describes the laboratory and field tests for the validation of the proposed UAS-AIR_T technique together with the mathematical framework developed to increase the SNR of IR images and improve the possibility of detecting subsurface voids.

2.1 Preliminary Evaluation of Environmental Parameters

Before performing the laboratory tests and narrowing down the environmental parameters replicated during the first part of the study, a review of the temperature of typical roadways and bodies of water was performed. Using the historical temperature data available, the monthly average temperature of 18 streams and rivers in Massachusetts has been evaluated for a period of one and a half years (i.e., from January 2019 to June 2020) *(77)*. Figure 2.1 shows the location of the bodies of water used for this analysis, Table 2.1 lists the rivers and streams surveyed, and Figure 2.2 is an example of the temperature trend by month for Hobbs Brook (ID 5) below the Cambridge Reservoir in Weston, Massachusetts over the period considered. The average monthly temperature for all the 18 bodies of water is included in Figure A.1 in Appendix A, together with the average temperature trend (see Figure A.2) and the web links to the temperature data sets (see Table A.1).

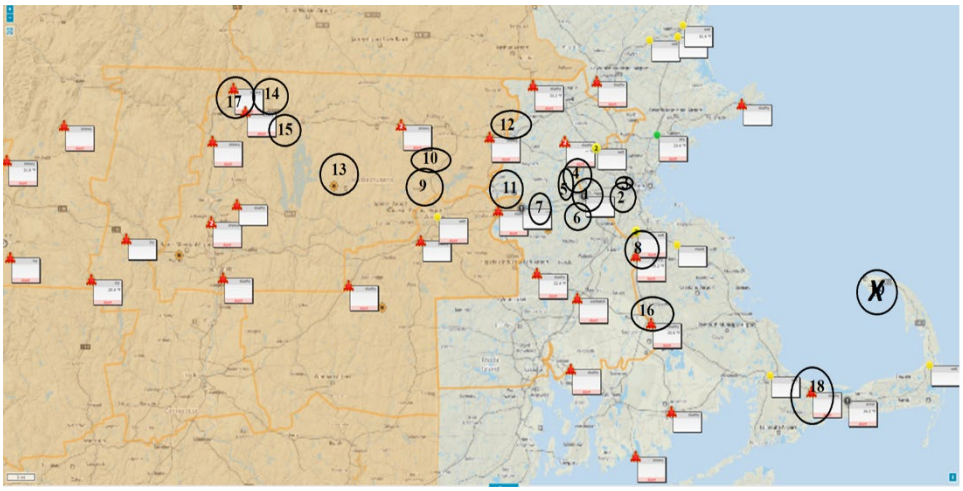

Figure 2.1: Locations of streams and rivers

Table 2.1: Bodies of water in this study

Body of water ID	Name	Location
1	Stony Brook at Route 20	Waltham, MA
2	Cambridge Reservoir: Unnamed tributary #3	Lexington, MA
3	Cambridge Reservoir: Unnamed tributary #1	Lexington, MA
4	Stony Brook at Viles Street	Weston, MA
5	Hoobs Brook below Cambridge reservoir	Weston, MA
6	Stony Brook: Unnamed tributary #1	Waltham, MA
7	Stony Brook: Unnamed tributary #1	Weston, MA
8	Tauton River	Bridgwater, MA
9	Still Water River	Sterling, MA
10	Quinapoxet River at Canada Mills	Holden, MA
11	Gates Brook	West Boylston, MA
12	Nashua River at Water Street Bridge	Clinton, MA
13	Ware River at Intake Works	Barre, MA
14	Green River	Colrain, MA
15	Connecticut River	Northfield, MA
16	Mill River at Spring Street	Tauton, MA
17	Old River	Florida, MA
18	Popponesset Bay at Mashpee Neck Road	Mashpee, MA

Road temperatures measured at locations closer to the bodies of water listed in Table 2.1 were used to determine the pavement's average monthly temperature over 2 years. Data from the Road Weather Information System (RWIS) stations highlighted in the map shown in Figure 2.3 were used for this purpose *(78)*.

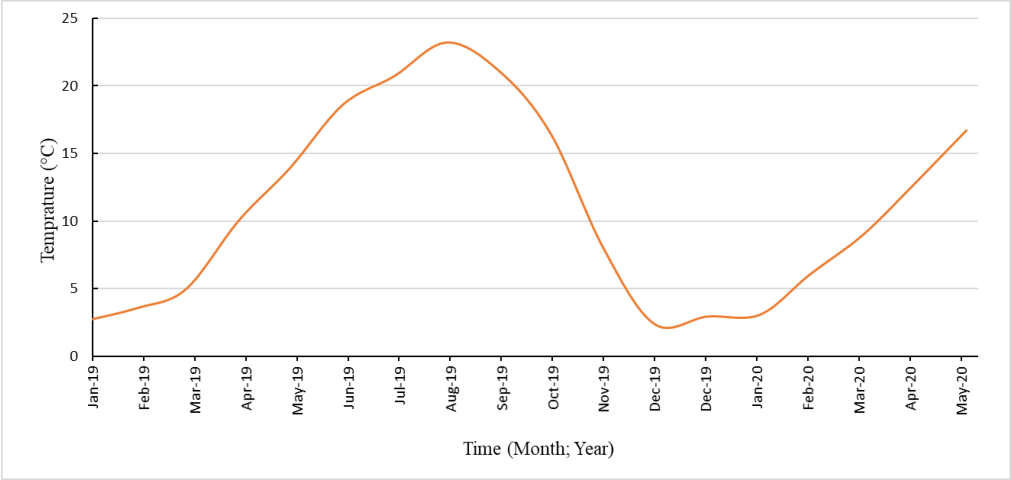

Figure 2.2: Average temperature in Hobbs Brook

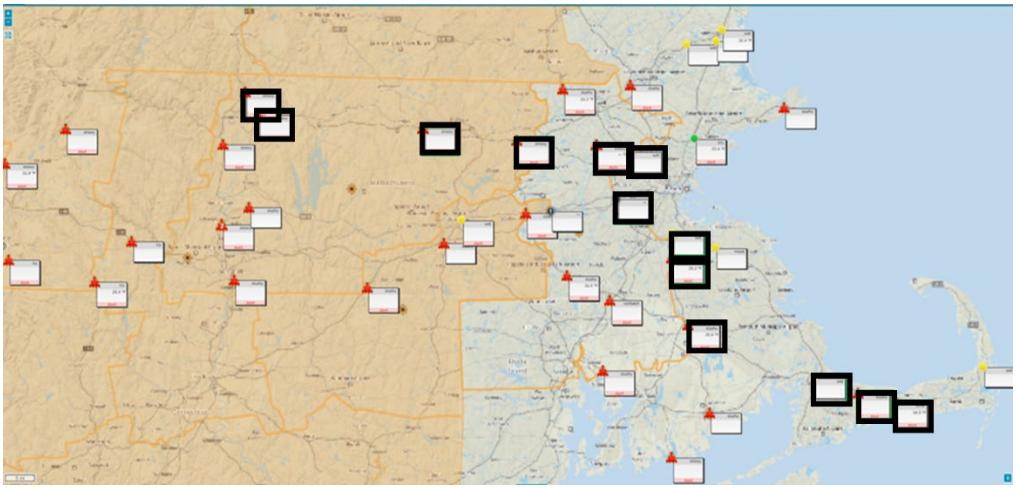

Figure 2.3: RWIS station locations

Analyzing the average temperatures for both bodies of water and roadways helps to identify the best season and time of the day characterized by a temperature differential between the roadway and the culvert that optimizes the thermal signature of the structure being tested and facilitates the detection of the damages. As observed in Figure 2.4, the average temperature of bodies of water is 9.69°C, with the minimum average being 1.80°C during February and the maximum average being 20.32°C in July. From Figure 2.4, it is also possible to observe that the minimum average temperature of the pavement is −0.75°C in December and the maximum average temperature is 32.50°C in July. The maximum temperature differential is then equal to 12.18°C, showing how better results can be obtained during the summer.

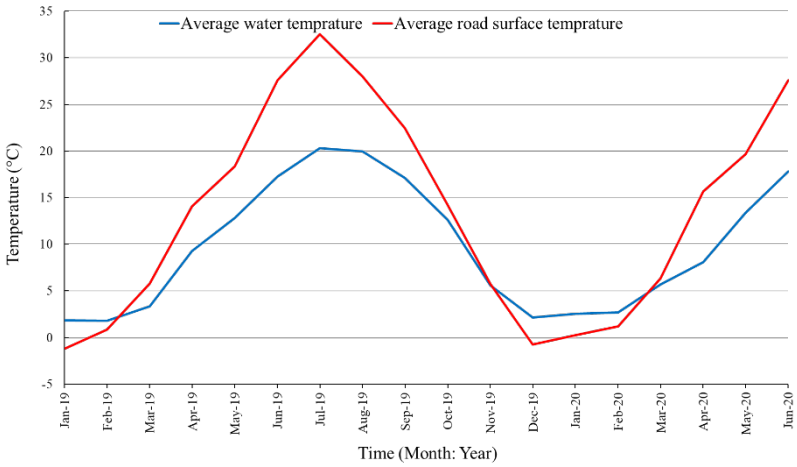

Figure 2.4: Pavement and water temperature differential

The values summarized in Figure 2.4 were then combined to determine the temperature difference and the maximum temperature of the roadway simulated during the laboratory experiments described in Section 2.2.

2.2 Experimental Setup for Laboratory Tests

Laboratory tests were performed to characterize the AIR_T system's capabilities to detect voids underneath a roadway in a controlled environment and with well-known boundary conditions. The objective of those tests was to investigate the smallest detectable defect size as a function of the IR camera's distance and tilt angle. The tests aimed at characterizing the detection accuracy of IRT as a function of (i) damage depth, (ii) moisture content, (iii) temperature difference, and (iv) IR method used (i.e., passive, active, and flash). A back-to-back comparison of the IRT results with those obtained from GPR analyses was also performed to characterize the accuracy of the proposed technique against currently used technologies. The laboratory tests were based on a laboratory-scale roadway on top of a metal culvert embedding defects that facilitate soil loss and the formation of subsurface voids. As shown in Figure 2.5, a 48 × 42 in. (~1.21 × 1.12 m) mock roadway with the stratigraphy based on the MassDOT standards for highways, roadways, and pavements was built (Figure 2.5a) *(79)*. An aluminized steel culvert having a nominal diameter of 30 in. (0.76 m) was installed in the structure ~20 in. (0.50 m) from the pavement surface (Figure 2.5b). An approximate 3 × 3 in. (0.08 × 0.08 m) damage was created on the top part of the pipe to mimic real-life damage and allow soil erosion from underneath the pavement (Figure 2.5c). The culvert was covered with 3/4 in. stone base and 1-1/12 in. dense-graded base soil to replicate the cross-section composition shown in Figure 2.5a. The soil was poured into the wooden box in approximately 3 in. (0.08 m) deep layers and compacted using a hand tamper and a jack compactor before adding the next layer. The pavement sample was installed on top of the last layer of soil to complete the experimental setup (Figure 2.5d).

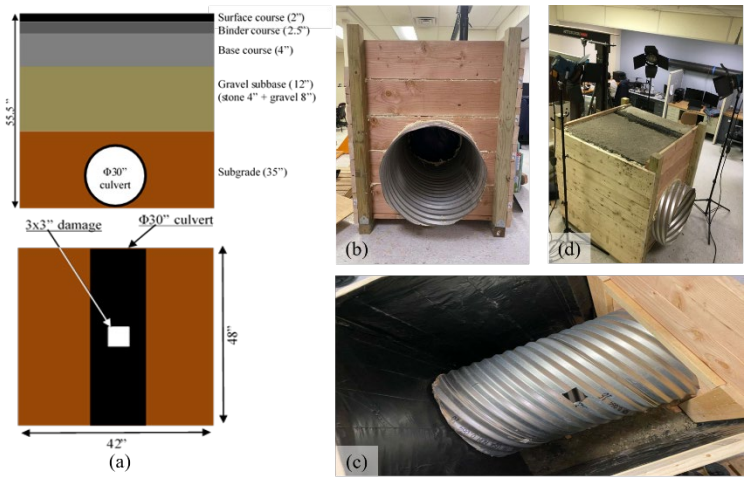

Figure 2.5: Laboratory test setup

In real-world scenarios, subsurface voids form as soil erodes from the subgrade and propagates through the gravel subbase and base course. The voids later reach the lower part of the road pavement, which becomes unsupported and then collapses with the whole structure. As shown in Figure 2.6a, the erosion process through the damage in the culvert phenomenon was recreated in the laboratory tests by removing a known quantity of soil. The soil was removed from the roadway's subgrade and subbase for each damage iteration until the defect reached the lower end of the pavement's base course. Voids with increasing volume representing more severe damage conditions D_i were simulated in this study (Figure 2.6b). In particular, four damage conditions having volume equal to $D_1 = 1.92 \times 10^{-3}$ m^3, $D_2 = 2.56 \times 10^{-3}$ m^3, $D_3 = 3.01 \times 10^{-3}$ m^3, and $D_4 = 3.33 \times 10^{-3}$ m^3 were considered. Each of those defects is shown in Figure 2.6c and had a surface (i.e., the planar projection of the damage in the roadway plane) equal to 0.19, 0.27, 0.32, and 0.41 m^2, respectively.

For all the tests described in this section, the IR system used consists of the Zenmuse XT2 IR camera manufactured by FLIR with a noise equivalent temperature difference (NETD) < 50mK and a thermal resolution of 640 × 512 pixels shown in Figure 2.7 *(80)*. The camera was fitted with a 13 mm focal length lens and positioned to have a working distance of 1.10 m (~43 in.) when in nadiral position (i.e., perpendicular to the road surface). The setup resulted in the camera's field of view (FOV) equal to 0.85 × 0.67 m (~2.80 × 2.20 ft) and ground sampling distance (GSD) resolution of 1.6×10^{-3} m/pixel (6.3×10^{-2} in./pixel). These values can be scaled linearly with the working distance for larger FOVs.

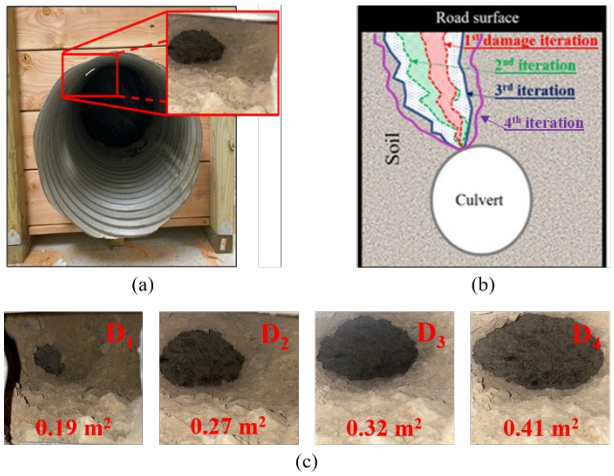

Figure 2.6: Subsurface voids of the culvert

Figure 2.7: FLIR Zenmuse XT2 IR camera

For each damage condition D_i, several tests were performed to characterize the IRT accuracy as a function of the

- type of IRT technique (i.e., passive and flash),
- IR camera's angle with respect to the road surface (i.e., 0, 15, 30, 45, and 60 degrees),
- effect of a tire's thermal signature on the IR images,
- effect of water on the road surface, and
- comparison with GPR.

The laboratory-scale roadway was lightened up for 1 s (flash) using a 1 kW halogen lamp before acquiring the IR images for the flash thermography test. For the passive IRT approach, the roadway was heated up for ~6 h to simulate sun heating and the images were taken as the surface was cooling down for 2 1/2 h. In both the flash and the passive IRT tests, the IR images were captured with the IR camera in five different orientations. In particular, tests with 0, 15, 30, 45, and 60-degree angles were performed. The camera had a 1 m distance from the roadway's surface when in nadiral position (i.e., 0 degrees). In addition, to simulate a tire's thermal signature and the effects of water on the roadway's surface, two other tests were

performed. To simulate the transit of a vehicle, a heating pad was used. The heating pad was left on the surface of the road for ~3 min before collecting the images with the IR camera tilted at 0, 15, and 30 degrees with respect to the surface of the roadway. Then, a known quantity of water was poured on the surface of the road before collecting three more images at 0, 15, and 30 degrees. A commercially available system developed by Geophysical Survey Systems Inc. was used for the back-to-back comparison with GPR. The UtilityScan GPR embeds 300 MHz and 800 MHz antennas, and scans at three different locations were performed during the tests. Two scans in corresponding undamaged parts of the roadway and one scan of a damaged part were performed. In particular, GPR scans at 11, 22, and 32 in. from the left edge of the mock roadway shown in Figure 2.5a were collected using both antennas. Figure 2.8 shows the setups used for performing the flash and passive IRT tests and the GPR scans, while a step-by-step summary of the test procedure is attached in Appendix B. Figure 2.8a shows the test setup for flash thermography accuracy as a function of camera angle; Figure 2.8b depicts the passive IRT setup showing the lights used to simulate sun heating of the road surface; and Figure 2.8c shows the setup for back-to-back comparison with GPR scans.

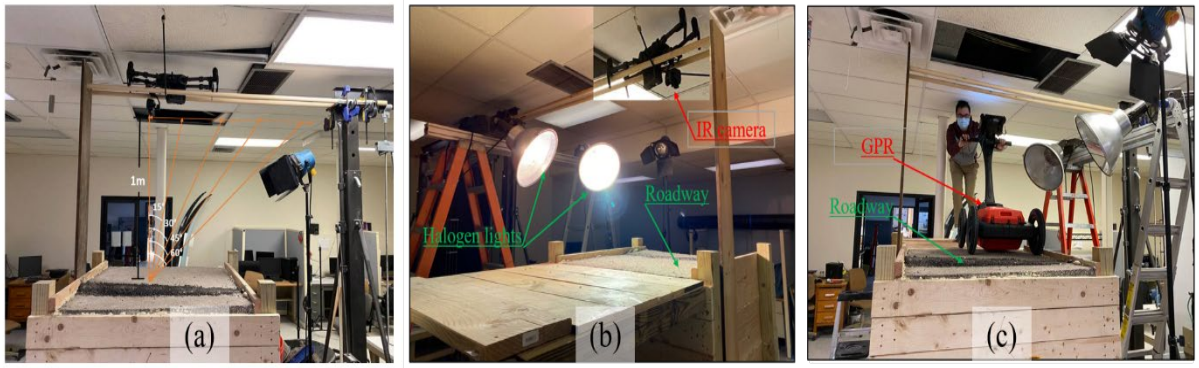

Figure 2.8: Experimental setups

A fan was used to extract air from the pipe and facilitate the heat exchange process to simulate outdoor conditions where the water flow through the culvert generates a temperature gradient. In particular, for the tests performed in this research, three different ventilation conditions were simulated: (i) 1-h continuous ventilation, (ii) 3-h continuous ventilation, and (iii) discontinuous ventilation. For the first two case studies, a fan was turned on to extract air from the culvert for 1 h and 3 h once the heating process was completed. For the third case study, the fan was turned on and off randomly while the roadway was cooling down and IR images were recorded.

2.3 Outdoor Validation Tests

To quantify the accuracy of the proposed UAS-AIR_T system in real-world scenarios, outdoor validation tests were performed. A field test program that includes the investigation of damaged and undamaged culverts was developed. In particular, the three locations indicated

in Figure 2.9 on Massachusetts Route 119 between Pepperell and Townsend, Massachusetts, were used as real-world testbeds. The selected culverts shown in Figure 2.10 represent systems that are (i) highly damaged and previously repaired (location 1), (ii) undamaged (location 2), and (iii) with damages having different severity (location 3). Figure 2.10a shows location 1, presenting a culvert with a partially collapsed ceiling that was repaired using an asphalt patch. Figure 2.10b shows location 2, an undamaged culvert; and Figure 2.10c shows location 3, a culvert with defects having different severity.

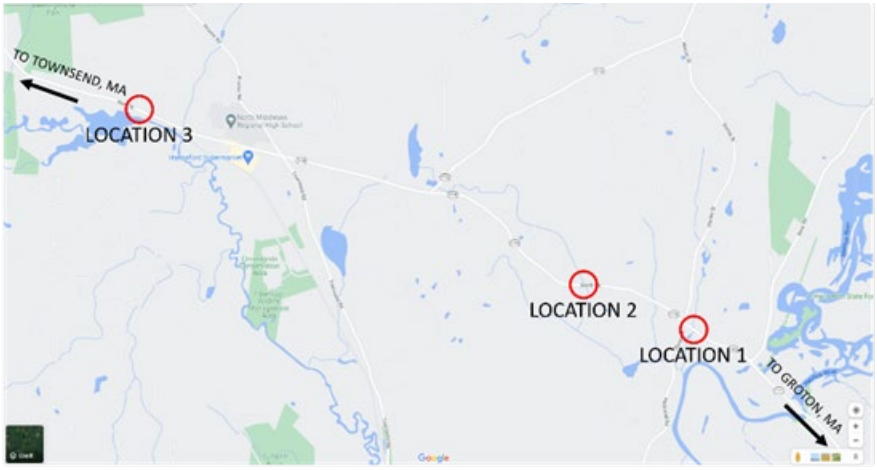

Figure 2.9: Culvert locations

Figure 2.10: Details of the three culverts

As shown in Figure 2.11, the outdoor tests were performed using a Federal Aviation Administration (FAA) registered DJI Matrice 200 V2 UAS (Figure 2.11a) manufactured by DJI and equipped with the same Zenmuse XT2 IR camera used for the laboratory tests *(81)*. The technical specifications of the UAS used in the tests are summarized in Table 2.2. During the tests, the UAS was remotely controlled by a certified pilot (Figure 2.11, b and c) and

operated according to the directives provided in the Small Unmanned Aircraft Regulations—Part 107 *(82)*.

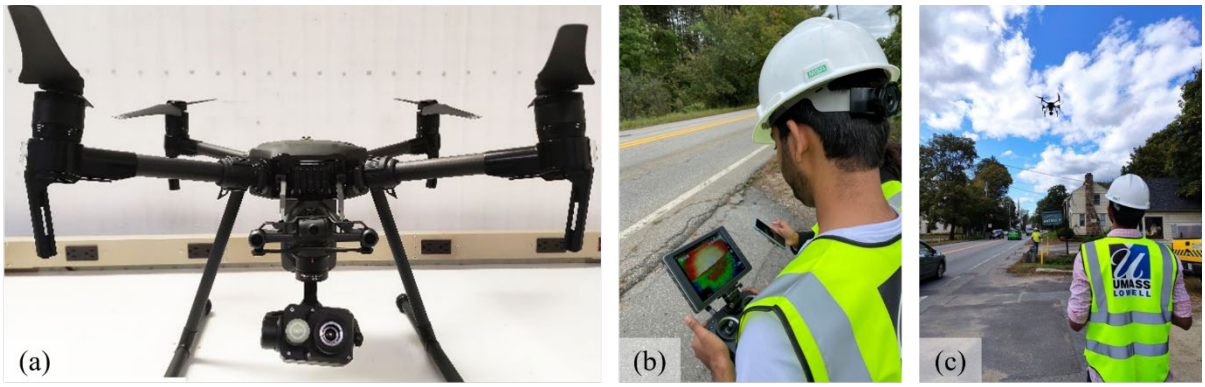

Figure 2.11: Equipment operated by remote pilot

Table 2.2: DJI Matrice 200 V2 technical specifications

Dimensions (mm)	883 × 886 × 398	Max flight time (min)	38 (no payload)
Diagonal (mm)	643	Max range (m)	5,000
Weight (kg)	4.69	Operating frequency 1 (GHz)	2.4000–2.4835
Max payload (Kg)	1.45	Operating frequency 2 (GHz)	5.725–5.850
Vertical accur. (m)	±0.1 (with DVS)	Battery capacity (mAh)	7,660
Horizontal accuracy (m)	±0.3 (with DVS)	Battery Type (–)	LiPo 6S
Max ascent speed (m/s)	5	Battery recharge (min)	~120
Max descent speed(m/s)	3	Battery weight (kg)	0.885
Max speed (km/h)	81 (or 61.2)	Battery swap time (s)	<60
Max wind (m/s)	12	Gimbal mounting (–)	Downward

The tests were performed at the beginning of October 2021 and divided over 3 days. On day 1, data were collected from all three locations by flying the UAS at an altitude of 50, 60, and 70 ft, respectively (15, 18, and 21 m, respectively). The goal was to determine the accuracy of IRT as a function of the GSD. During the first day, IR images were collected at 30-s intervals by hovering the UAS on the edge of the roadways for 8 min (total of 16 IR images). On day 2, two different image collection protocols were used. In the first approach, one IR scan was collected with the drone flying at an altitude of 15 m at location 1 before moving to location 3 to acquire another image. Then the same procedure (i.e., photo at location 1 first and photo at location 3) was repeated for a total of six flights per location to have enough data to perform image processing. The goal was to allow for a longer time interval between subsequent images at the same location and simulate a possible data collection procedure for MassDOT personnel. The second approach involved six preplanned flights performed at location 3 at intervals of ~15 min from each other. The UAS was flown between point A and point B (Figure 2.12) to collect IR images with 90% overlap to reconstruct the orthomosaic of the area. During this approach, a total of six orthomosaics were generated. The objective of this test was to obtain enough temporal data for implementing the image post-processing framework described in

Section 2.3. A 90% overlap is a required specification to increase the number of points common in two adjacent photos and facilitate the orthomosaic stitching process.

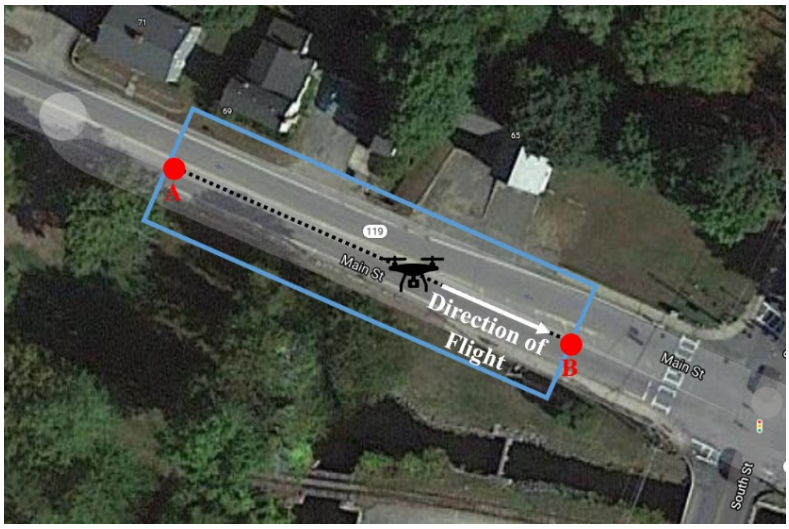

Figure 2.12: Preplanned flight path

On day 3, the flights were conducted at night at location 3 to avoid sun shadows and maximize the temperature gradient between the roadway and the water in the culvert. All flights performed during the third day were carried out with a preplanned flight mission with a 15-min delay between subsequent flights, similar to Approach 2 used during the second day of tests. A detailed step-by-step summary of the outdoor test procedure is attached in Appendix C.

2.4 Advanced IR Images Post-Processing Techniques

Despite the growing use of IRT for civil infrastructure monitoring and subsurface damage detection, flaws and defects are not always captured in IR images when radiometric photos are inspected. Even after using traditional image processing techniques such as image derivatives, defects remain undetected frequently *(83,84)*. For these reasons, different approaches based on advanced image post-processing techniques and reduced-order models are discussed in this research to increase the SNR of the images and facilitate the detection of subsurface voids. The techniques used in this study were (i) R2-based analysis, (ii) PCT, and (iii) sparse-principal component thermography (S-PCT). This section describes the mathematical framework on which each of those techniques is based.

2.4.1 R^2-Based Analysis

According to Newton's law of cooling, when a warmer object is kept in a colder environment, its temperature decreases until it reaches thermal equilibrium with the surroundings. If there is any difference in the cross-sectional area, such as a change in thickness or a structural

discontinuity, the cooling curve at that specific location is different. As a result, the temperature decay curve's coefficient of determination (COD or R^2 value) is higher at that location *(85)*. For example, if a defect such as a void or a cavity is present in the object, that area should cool down at a higher rate than undamaged regions. That temperature difference causes an increase in the R^2 value of the curve fitting the temperature profile of the area characterized by the damage. In this research, the temperature was collected from IR images while the roadway was cooling. Temporal series of thermal data were fitted with an exponential function. In particular, IR images of the roadways were collected over time (i.e., t_1, t_2, …, t_{n-1}, t_n) and the temperatures were extracted from each IR image using FLIR thermal studio software. To reduce the computational time and take into account small motions of the IR camera, the temperature of each pixel was calculated as the average of a 3 × 3 kernel around the pixel itself (Figure 2.13a). The same procedure was replicated for all the N images of the time series to generate the temperature decay of each pixel over time (Figure 2.13b). For every averaged pixel, the temperature profile was fitted using an exponential curve, and the R^2 value of the pixel was determined. An R^2 plot similar to the one shown in Figure 2.13c can be obtained by repeating the same procedure for each pixel.

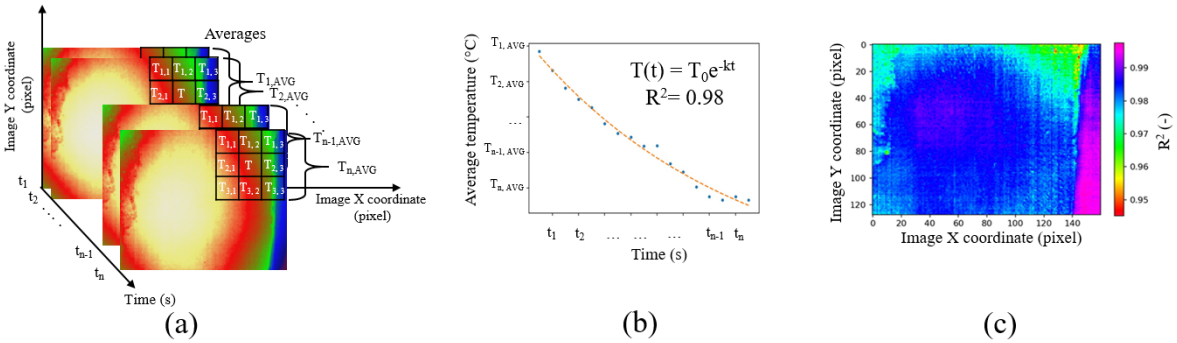

(a) (b) (c)

Figure 2.13: Workflow of the R^2-based analysis

The R^2 value distribution plot similar to the one shown in Figure 2.13c can be used to determine the presence of a defect in the object. Every increase in the R^2 values compared to the adjacent pixels is representative of a change in the local thermal properties of the object and indicate the location of a defect. The R^2-based algorithm has been developed in Python, and the code used for analysis is attached in Appendix D.

2.4.2 Principal Component Thermography and Sparse-Principal Component Thermography

The principal component analysis (PCA) is a statistical method that allows identifying variance present in a data set *(86)*. Characteristic features such as similarities or differences in the patterns can be separated through the statistical modes using singular value decomposition (SVD) *(87)*. Among different applications in the dynamics domain, PCA has been used as a post-processing algorithm to extract statistical modes from IR images. It has been referred to as PCT *(88)*. The extracted statistical modes represent variation and changes in temperatures around the defects over time *(89)*. To perform PCT, a time series of IR images captured at times $t_n = t_1, t_2, \ldots, t_{n-1}, t_n$ and similar to the ones shown in Figure 2.14a is needed. Each image

has i columns (x-direction) and j rows (y-direction) so that the number of pixels goes from i = 1 to n_x in the x-direction and from j = 1 to n_y in the y-direction. Before performing PCT, each IR image is rearranged to create a time-vector $\mathbf{T_n}$ with $k_x \times k_y$ elements as shown in Equation (1):

$$\mathbf{T_n} = (T_1, T_2, T_3, ..., T_{kxky})_n \tag{1}$$

where the elements T_1, T_2, T_3, …, T_{kxky} represent the temperature values of the pixels at time n. All the IR images' vector $\mathbf{T_n}$ are then arranged in a $(k_x \times k_y) \times n$ matrix $\underline{\mathbf{A}}$ similar to the one shown in Figure 2.14b.

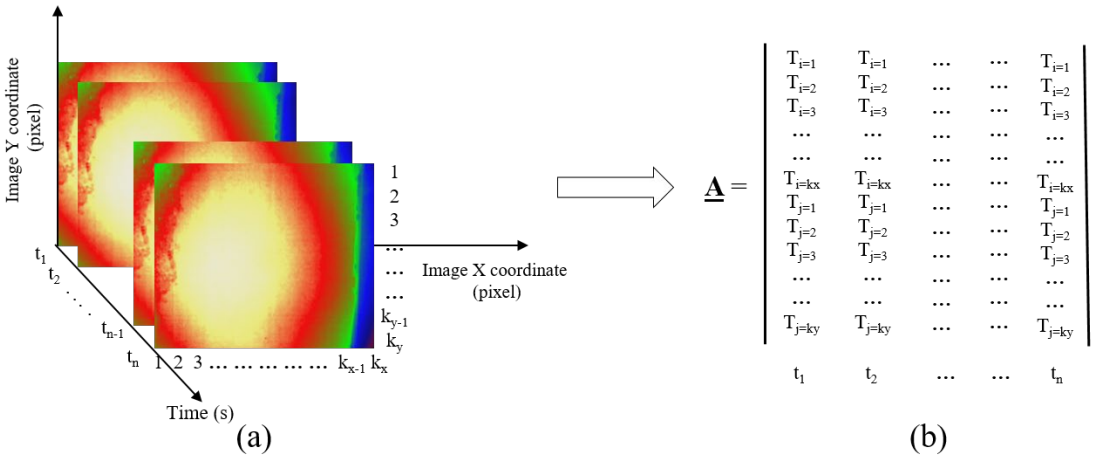

Figure 2.14: PCT workflow

The covariance (COV) of the normalize data is calculated with Equation (2):

$$\mathbf{COV} = \frac{1}{t_n} \boldsymbol{A}\boldsymbol{A}^T \tag{2}$$

where $\mathbf{A}$ is the $(k_x \times k_y)$ x t_n matrix after normalization of $\underline{\mathbf{A}}$. Eigenvalues and eigenvectors of the matrix $\mathbf{A}$ can be calculated using Equation (3):

$$\mathbf{COV}_D = \boldsymbol{P}^{-1}\, \mathbf{COV}\, \boldsymbol{P} \tag{3}$$

with COV_D being the diagonal matrix of the eigenvalues of the normalized matrix $\mathbf{A}$ and $\mathbf{P}$ is a matrix with eigenvectors as column elements. All the orthogonal modes $\mathbf{U}$ (are also referred to as empirical orthogonal functions [EOFs]) that are representative of defects can be computed using Equation (4):

$$\boldsymbol{U} = \underline{\boldsymbol{A}}(\boldsymbol{P}^T)^{-1}(\mathbf{COV}_D)^{-1} \tag{4}$$

PCT is a linear decomposition method and is sensitive toward outliers and signal noise. This problem is common to all the different types of PCT *(90, 91)*. A modified version of PCT,

known as sparse-principal component thermography (S-PCT), has been developed to address nonlinearity and latent variables *(92–94)*. PCT and S-PCT techniques are well established to identify defects in different applications *(95–97)*. However, it was shown that the S-PCT performs better when the system is nonlinear and critical information resides in sparse variables. The preprocessing step of S-PCT is similar to the PCT one, which is given in Equation (1). The main difference is that the principal components of S-PCT are extracted using an optimization problem based on the total number of non-zero elements in the temperature vector (L_0) and the sum of all absolute values in a vector (L_1). By considering non-zero elements and the sparsity characteristics of the thermal distribution, the method is more robust. The PCT and S-PCT algorithms have been developed in Python, and the codes used for analysis are attached in Appendix E.

An implementation of S-PCT was performed on composite structure and demonstrated better damage detection capabilities than PCT *(98)*. Because both PCT and S-PCT provide results as a function of the time interval used to sample the images, this study also evaluated the sensitivity of these two techniques for different time capturing intervals. In particular, images were recorded at intervals of (i) 2 min, (ii) 5 min, (iii) 10 min, (iv) 15 min, and (v) mixed (i.e., a combination of the previous four). The mixed interval is proposed based on practical considerations to collect more meaningful data for real-world applications. As the roadway begins to cool down, the temperature decay rate is faster at the beginning and reduces over time. If the image-capturing interval is kept constant, the thermal information during the initial cooling stages (i.e., the steepest part of the exponential cooling curve) might get lost. Also, it might be challenging to collect the data at specific time intervals in real-world culvert inspection. To overcome the drawbacks mentioned above, the mixed time interval is proposed and its accuracy is evaluated and compared to the other fixed-time measurements. With the mixed time interval, IR images are initially collected at a faster rate (e.g., every 30 s for the first 5 min). Then, the image collection rate decreases while the object's temperature approaches the thermal equilibrium with the surrounding environment.

This page was left blank intentionally.

3.0 Results

In this section, the outcomes of the tests described in Sections 2.2 and 2.3 are analyzed. In particular, the accuracy of the UAS-AIR_T method is validated using the traditional first and second derivative approaches, compared to GPR, and using the three advanced post-processing techniques described in Section 2.4.

3.1 Analysis of the GPR Data

The GPR testing was conducted by performing six GPR B-scans at three different locations corresponding to two undamaged parts of the roadway and one damaged part. The data collected with the GPR system at the frequencies of 300 and 800 MHz were processed, and an example of the results obtained is shown in Figure 3.1. In the GPR B-scan images, the *x*-axis is the length of the inspected portion of the road (i.e., ~10 in.) with backscattered signal recorded by the GPR in the direction of the scan, whereas the *y*-axis represents the depth of the structure.

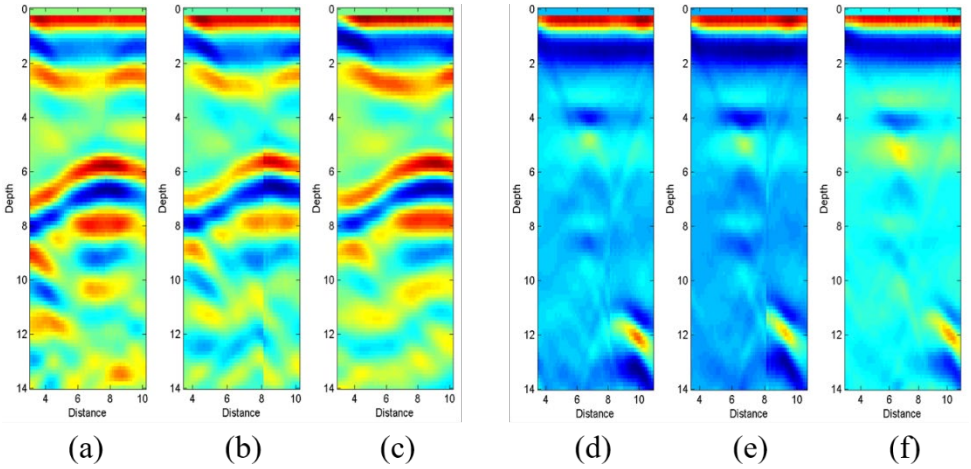

Figure 3.1: B-scans at 300 and 800 MHz

Detectability of defects with GPR is highly sensitive to the dielectric contrast between two materials. As the subsurface layered structure in the experimental setup is not uniform (Figure 2.5a), the dielectric constant varies from one layer to another, affecting the quality of the collected GPR B-scan images. With the current GPR system, only a single dielectric constant value can be assumed in each GPR scan, inducing a ranging error in the reconstructed images. From the analysis of the GPR B-scan images, it is possible to observe that 300 MHz provides the best results in locating the top wall of the culvert (Figures 3.1a–c). In contrast, the 800 MHz antenna can provide qualitative information about the location of the subsurface void (Figures 3.1d–f). However, the detection of damages from the scans shown in Figure 3.1 is not univocal. It leaves room for contrasting opinions based mainly on the experience and expertise

of the inspector analyzing the images. For this reason, no conclusive results can be drawn from the GPR analysis.

3.2 Analysis of IR Images Processed with Traditional Methods

Data collected with the FLIR Zenmuse XT2 IR camera during the laboratory tests were first processed using traditional image processing techniques such as image first and second derivatives. In these methods, the first and second derivatives of the intensity value across the image are calculated to find points where the derivative values are maximum and represent edges. The derivative operator allows determining the gradient of the image that is a vector whose components measure how rapid pixel values (i.e., the temperature in the specific case study) change with distance in the *x*- and *y*-directions. Thus, IR images collected while the roadway was cooling down were processed to calculate temperature gradients representing defects. The data were collected with the camera in the nadiral position (i.e., 0 degrees) with

- no obstructions on the surface of the roadway (Figure 3.2a),
- a heating pad to mimic the thermal signature of a tire (Figure 3.2b), and
- with water on the surface of the roadway (Figure 3.2c).

An example of the raw IR images collected for those three scenarios is shown in Figure 3.2.

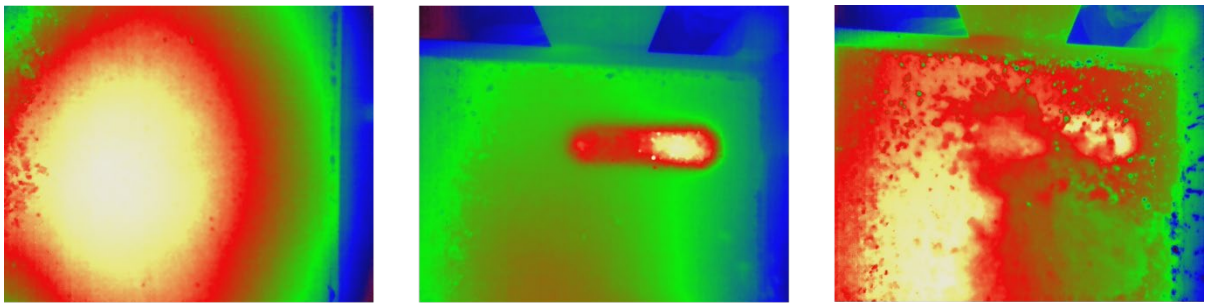

(a) (b) (c)

Figure 3.2: Raw IR images

When the raw IR images were processed and the first and second derivatives calculated, the results shown in Figures 3.3 and 3.4 are obtained. For the case shown in Figure 3.3, three IR images were collected once the heating process was completed (Figure 3.3a), after 40 min (Figure 3.3b), and after 80 min (Figure 3.3c). The goal was to prove that results were not a function of the time images were taken. From the analysis of Figure 3.3, it is possible to observe that the thermal shadow of the halogen lamps used for warming up the surface that creates an uneven thermal distribution was the only feature visible in the derivatives even after 80 min. No subsurface defects were visible when images' first and second derivatives are analyzed. Similar conclusions can be drawn for the other two case studies (i.e., thermal signature of tires and water on the pavement) shown in Figure 3.4.

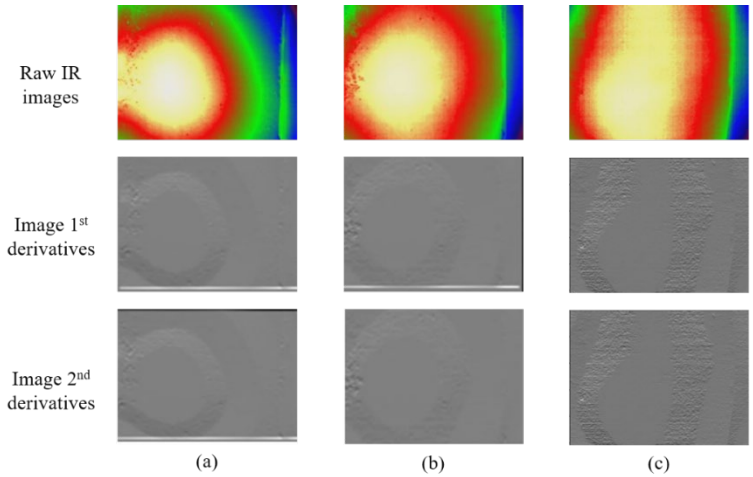

Figure 3.3: Derivatives 0–80 min after halogen lamp

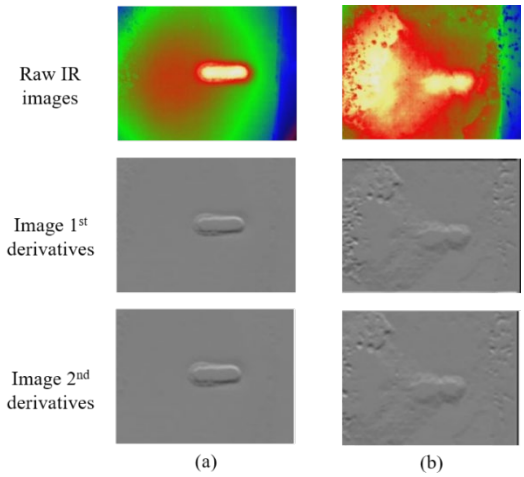

Figure 3.4: Derivatives with heating pad and surface water

It was observed how in the cases of the tire thermal signature and water on the surface of the roadway, the higher temperature of the heating pad or the change of emissivity caused by the water reduced the quality of the processed images significantly and masked any subsurface defect. When the gradient of the IR photos was calculated, the SNR of the images dropped significantly, making the detection of subsurface defects difficult. For those reasons, advanced image processing techniques were used to improve the accuracy of the UAS-AIR_T method.

3.3 Analysis of IR Images Processed with Advanced Methods

The IR images of the four damages D_1, D_2, D_3, and D_4 and the three ventilation conditions were processed with the R^2-based analysis by implementing the Python code attached in Appendix D. The average temperature value of each 3×3 pixel kernel in the IR images was calculated and used to generate the cooling curve of each kernel. The obtained data were then fitted with an exponential curve to determine the R^2 value. The R^2 value maps obtained for the considered damages and ventilation conditions are shown in Figure 3.5.

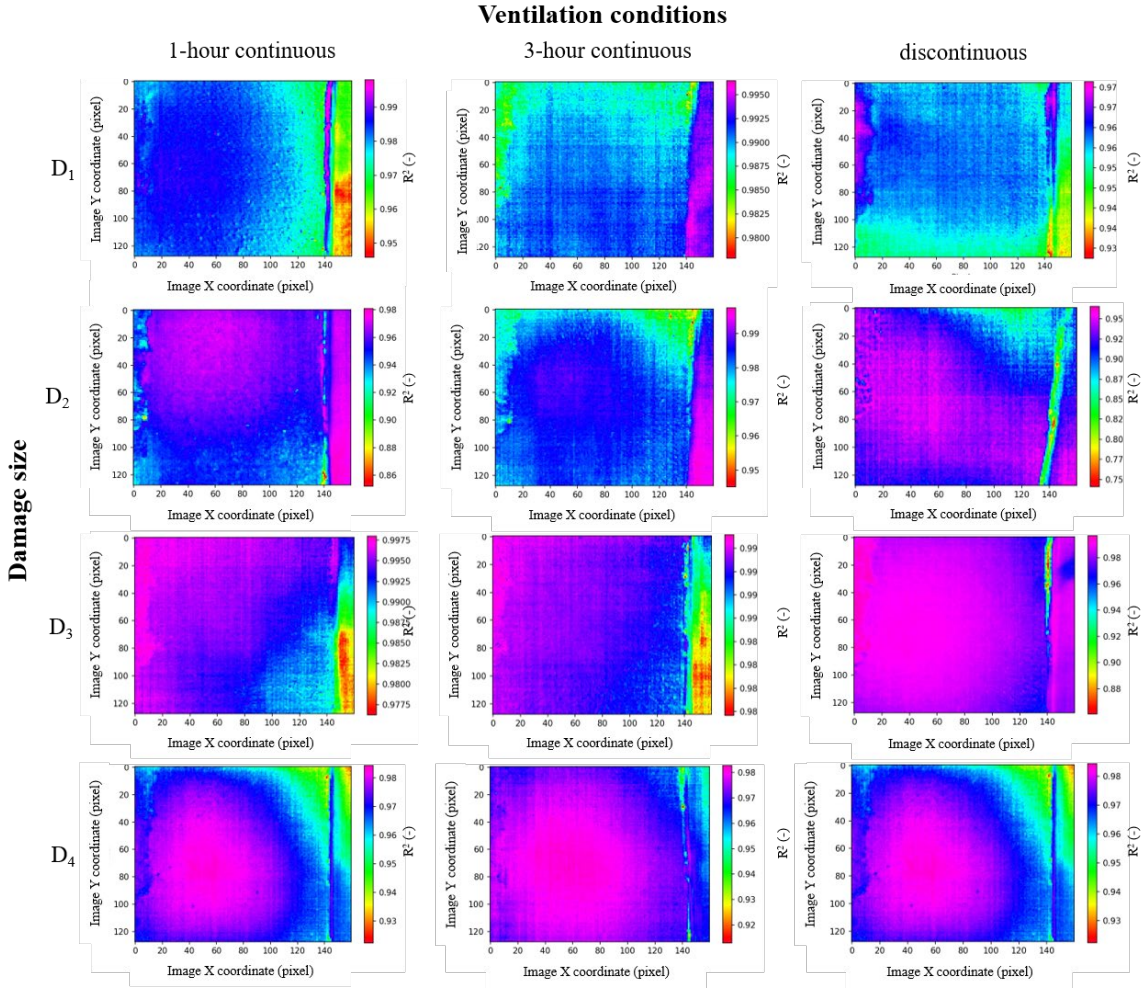

Figure 3.5: R^2-based results showing COD distributions

As observed from the analysis of the plots shown in Figure 3.5, the R^2-based analysis was able to locate the approximate location of the larger defect (i.e., D_4) only without providing accurate information about the size of the defect that seems to be overestimated if compared to the actual size of the void. In addition, successful recognition of the defect was possible only for the 1-h and the discontinuous ventilation conditions. For the smaller defects (i.e., D_1, D_2, and D_3), the R^2-based analysis did not detect any variation in the thermal transmissivity of the roadways. This approach did not prove to be sensitive enough to identify defects that do not significantly affect the thermal property of the system, resulting in more significant variation from the ideal cooling curve.

When the IR images were processed with PCT and S-PCT analyses using the steps described in Section 2.4.2 and the Python code attached in Appendix E, the second empirical orthogonal functions ($EOFs_2$) shown in Figures 3.6 and 3.7 were obtained. The results presented demonstrate that PCT can identify the subsurface voids shown in Figure 3.6 by the red contours. Although the detection accuracy increased compared to the R^2-based analysis, results obtained with the PCT were not always consistent. In particular, damage D_1 was visible for all three ventilation conditions, but damage detection for scenarios D_2 and D_3 was not always possible. Figure 3.6 shows that the thermal shadow of the void for damages D_2 and D_3 was partially visible but not as evident as for damage D_1. Moreover, PCT-based analysis was not able to locate the damage in any ventilation conditions for damage D_4. For this last scenario, a more prominent spot in correspondence of the subsurface void can be observed. However, its boundaries are not well defined and the transition between areas with different thermal properties (i.e., damaged vs. undamaged) is not as sharp as expected. Figure 3.7 presents the EOF_2 obtained when the IR images are processed using S-PCT. Unlike PCT, S-PCT was able to identify defects in all the damage size and ventilation conditions. In all the scenarios analyzed, S-PCT has proven to be the most robust post-processing method to identify voids underneath the roadway. As observed in Figure 3.7, damages can be identified by a red spot in the thermogram.

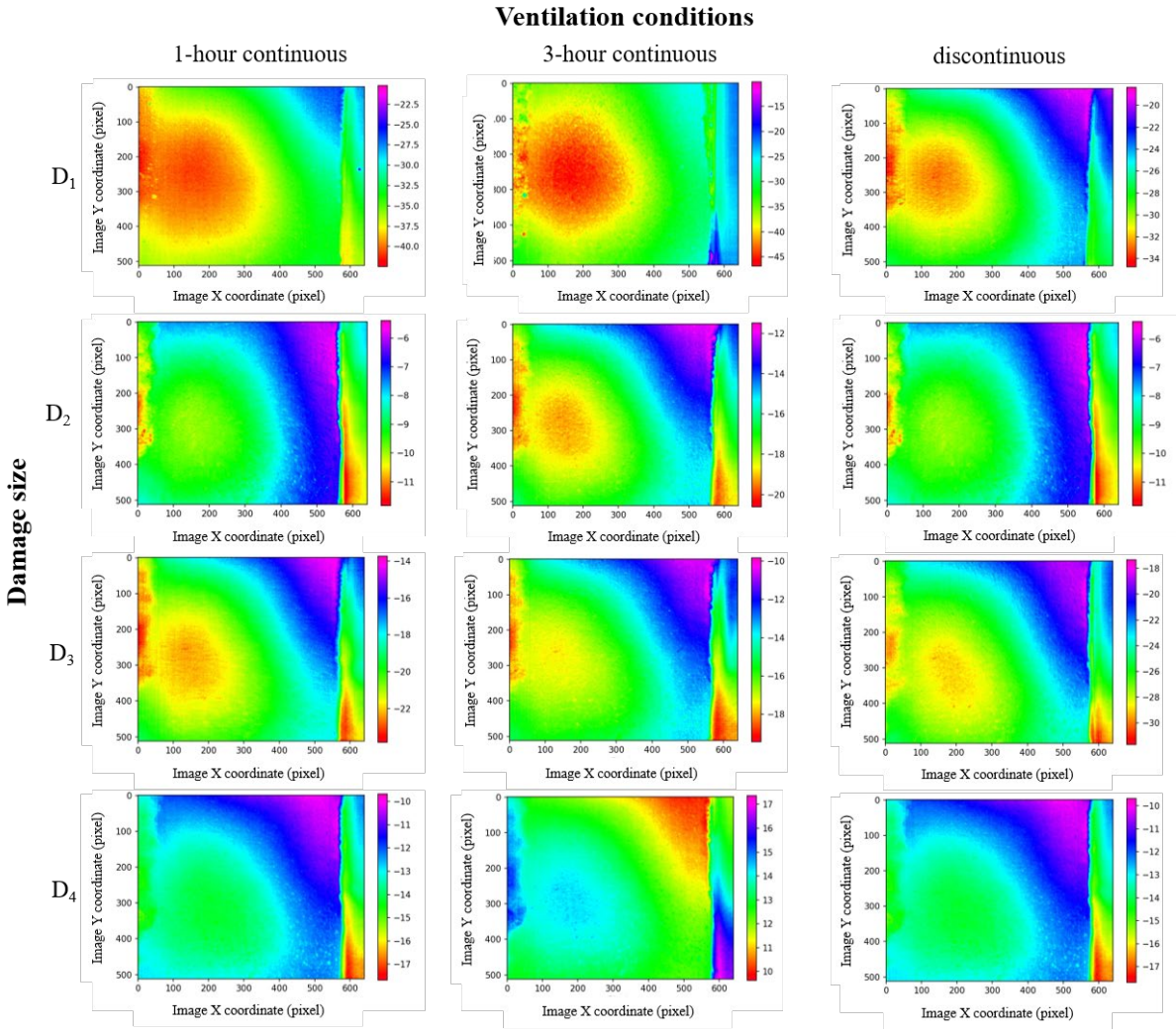

Figure 3.6: EOF_2 from PCT analysis

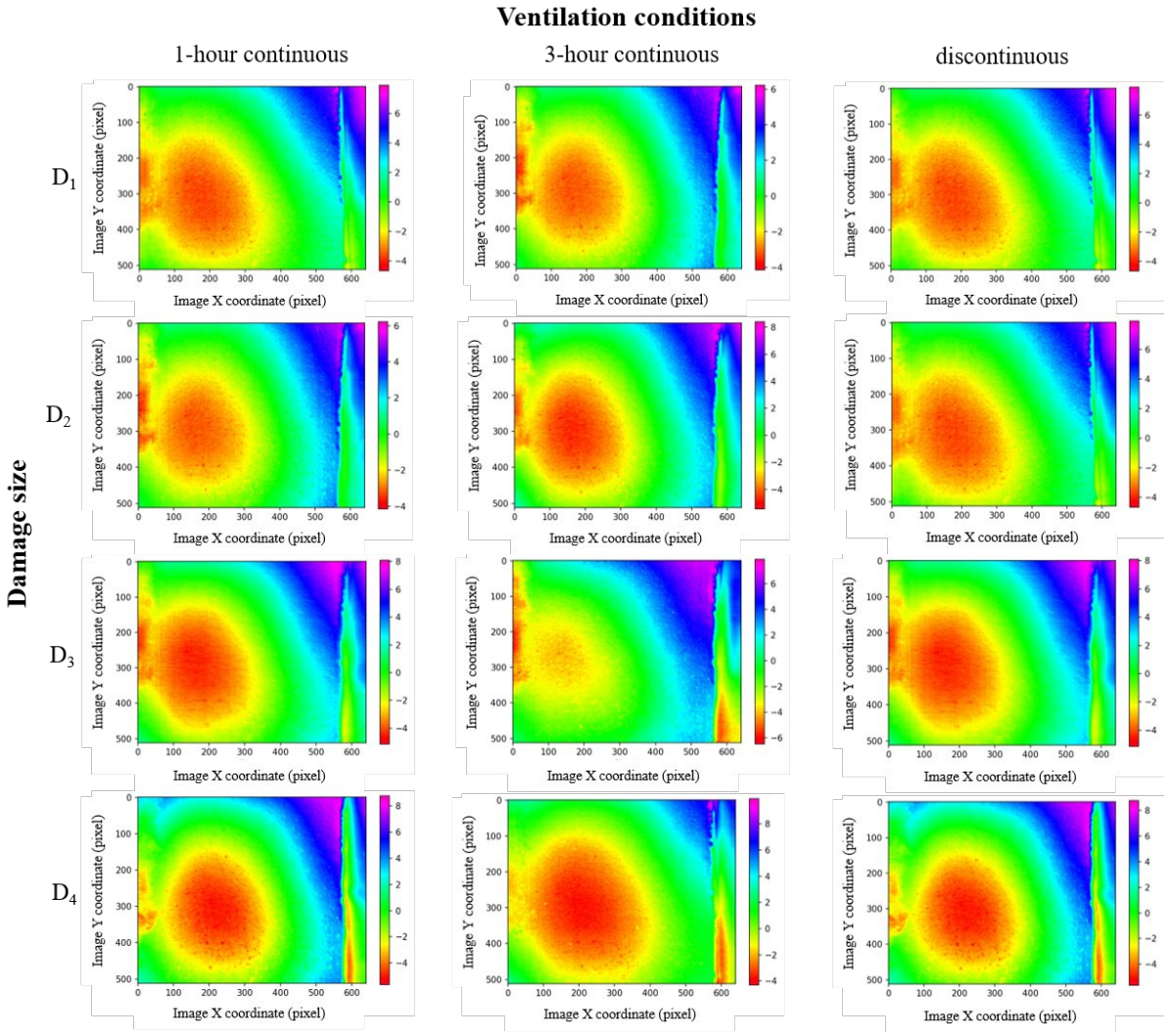

Figure 3.7: EOF$_2$ from S-PCT analysis

The accuracy of the three methods was assessed by measuring the size of the defects as represented in the images.

Table 3.1: Accuracy of the three techniques

		1-h continuous			3-h continuous			discontinuous		
		R^2	PCT	S-PCT	R^2	PCT	S-PCT	R^2	PCT	S-PCT
Defect	**Surf. (m^2)**	ε_r (%)	ε_r (%)	ε_r (%)	ε_r (%)	ε_r (%)	ε_r (%)	ε_r (%)	ε_r (%)	ε_r (%)
D_1	0.19	—	21.05	15.78	—	15.78	5.26	—	5.26	31.57
D_2	0.27	14.00	—	22.23	85.1	71.42	11.12	88.89	—	14.81
D_3	0.32	67.74	52.94	14.7	77.41	94.11	55.87	—	82.35	8.82
D_4	0.41	51.21	—	31.7	78.04	—	9.75	58.58	—	21.95
Average (%)		**44.32**	**37.00**	**21.10**	**80.18**	**60.44**	**20.50**	**73.74**	**43.81**	**19.29**

The areas of the defects in the images are compared to the actual surface of the defects obtained by projecting the contour of the void in the image plane. Table 3.1 summarizes the relative error, ε_r obtained as a function of defect size and ventilation conditions using R^2-based analysis, PCT, and S-PCT. As observed from the data summarized in Table 3.1, the percent errors for S-PCT for all defect sizes and ventilation conditions is significantly smaller when compared to the results obtained with R^2 and PCT. It proves that S-PCT can detect defects independently of their size and provide more accurate quantification about the size of the void. The R^2-based analysis works better for more significant defects, whereas PCT is more effective when smaller defects need to be observed. Errors in the order of ~20% can be caused by a nonperfect overlap between the pavement base course and the gravel subbase that results in smaller voids that affect the heat transmission but are not quantified and taken into account when the physical surface of the void is measured (Figure 3.8).

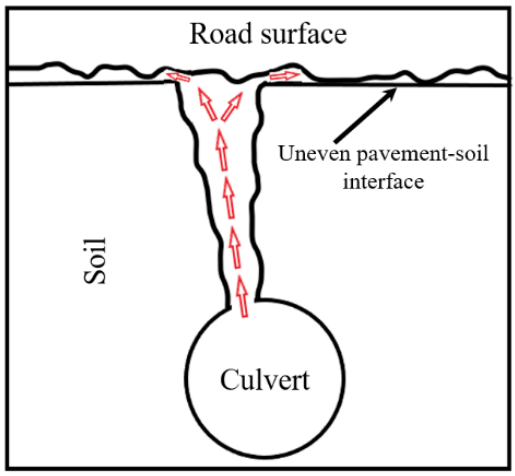

Figure 3.8: Uneven pavement–soil interface

3.3.1 Time Sensitivity Analysis

SVD techniques are sensitive to the time intervals used to acquire data. Because the sampling rate of IR images may vary due to traffic conditions, the sensitivity of PCT and S-PCT as a function of the time in between subsequent images is assessed. Five different time intervals were used: (i) 2 min, (ii) 5 min, (iii) 10 min, (iv) 15 min, and (v) mixed (i.e., a combination of the previous four). The results of this analysis are shown in Figure 3.9. It is observed that the R^2-based analysis does not allow identifying any defect. In the case of PCT, the patch indicating the defect was most clearly visible when a faster sampling rate was used (i.e., 2 min). As the sampling rate decreases, the clarity of the patches representing the thermal signature of subsurface void decreases and the possibility to identify the defects is reduced. PCT was found to be highly sensitive toward the time capturing interval. In the case of S-PCT, the defect was easy to identify for every time interval under consideration.

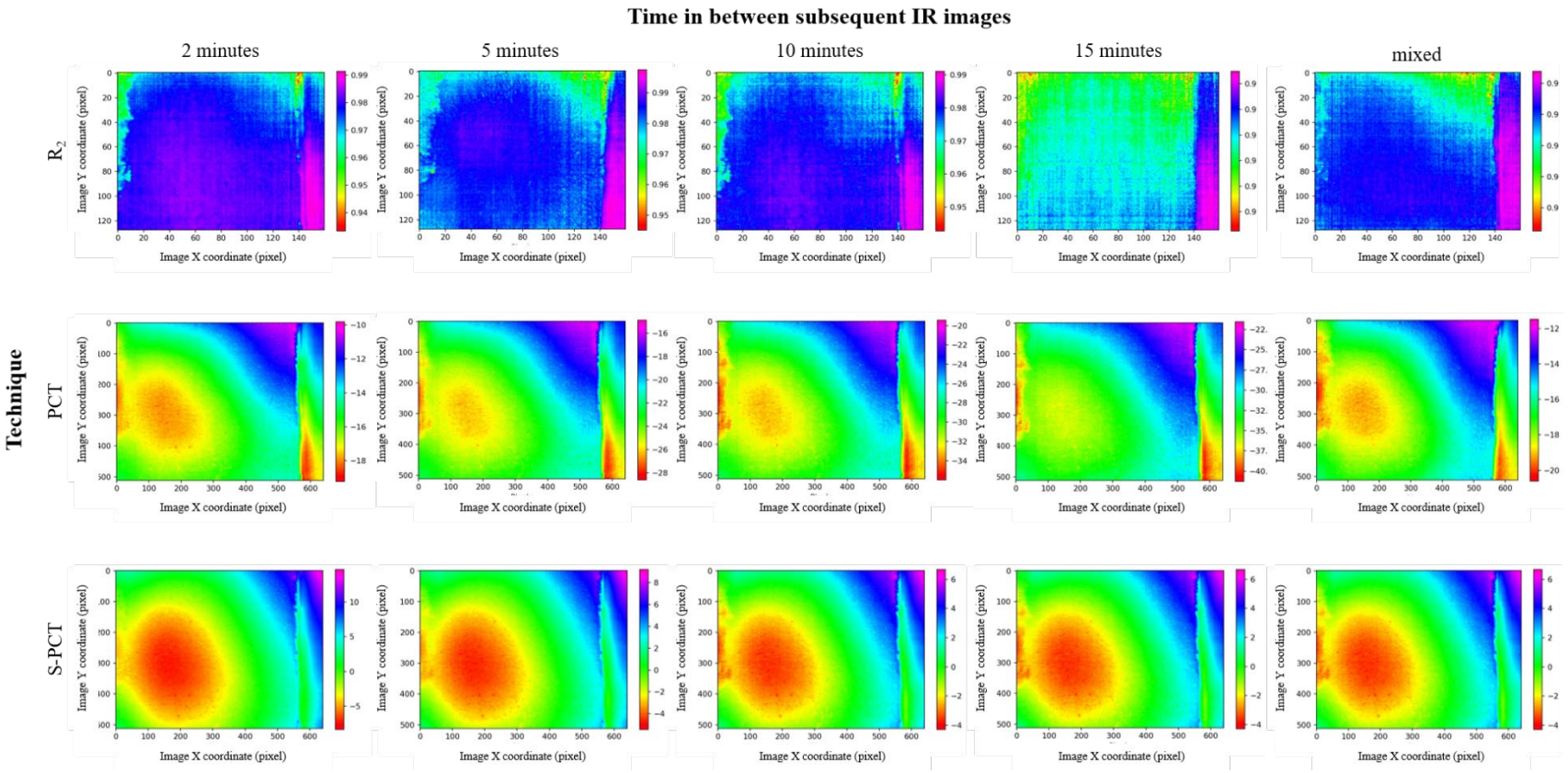

Figure 3.9: IR images comparing technique and time

However, because collecting images every 2 or 5 min throughout the cooling process may not be feasible, a mixed sampling rate can also be used to locate the defect with enough accuracy. The accuracy of the three techniques is summarized in Table 3.2, where the relative error ε_r as a function of the sampling rate is shown.

Table 3.2: Accuracy as a function of sampling rate

	Sampling rate (minutes)					
	2	**5**	**10**	**15**	**mixed**	**Average**
Technique	ε_r (%)	ε_r (%)	ε_r (%)	ε_r (%)	ε_r (%)	(%)
R^2-based	64.97	85.10	70.37	—	—	73.48
PCT	33.32	55.50	62.96	77.78	44.40	54.79
S-PCT	3.70	7.40	14.81	18.51	11.10	11.10

3.4 Analysis of the Outdoor Performance Tests

As suggested from the results of the laboratory tests, PCT and S-PCT provide better results for detection of subsurface voids. Hence for all the outdoor tests, the data were analyzed with PCT and S-PCT only. An example of the IR images collected during the outdoor tests for the three locations inspected is shown in Figure 3.10: a sinkhole fully opened and repaired at location 1 (Figure 3.10a); an undamaged culvert at location 2 (Figure 3.10b); and sinkholes forming at location 3 (Figure 3.10c).

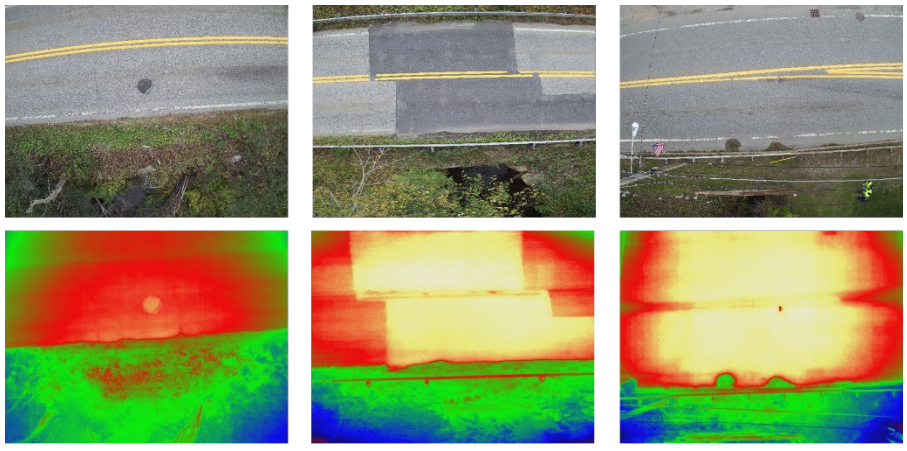

Figure 3.10: IR images of the three culverts

During the first set of outdoor tests performed, the IR images were taken by hovering the UAS at different altitudes for determining the detection capabilities of the UAS-AIR_T systems as a function of the GSD. The UAS hovered at location 1 at altitudes of 15, 18, and 21 m (50, 60,

and 70 ft) while IR images were collected every 30 s with flight details summarized in Table 3.3. The results of PCT and S-PCT analyses for location 1 with defect on the roadway highlighted and on IR images collected at 15 m (50 ft) altitude (Figure 3.11a); 18 m (60 ft) altitude (Figure 3.11b); and 21 m (70 ft) altitude (Figure 3.11c). As observed from the thermal maps, the defect is visible in the images processed with both techniques. As the flight altitude and GSD increase, the size of the damage reduces, but it is still clearly visible in the images. For defects that are visible on the roadway's surface, both PCT and S-PCT can identify the location of the damage. The only difference is that the defect's edges are more pronounced when S-PCT is used.

Table 3.3: Flight details to determine IRT accuracy

Flight details (per altitude)					
No. of flights (-)	Duration (min)	Sampling rate (s)	Time (hh:mm)	Air temp. (°C)	Water temp. (°C)
3	8.0	30.0	1:00 p.m.	20.0	10

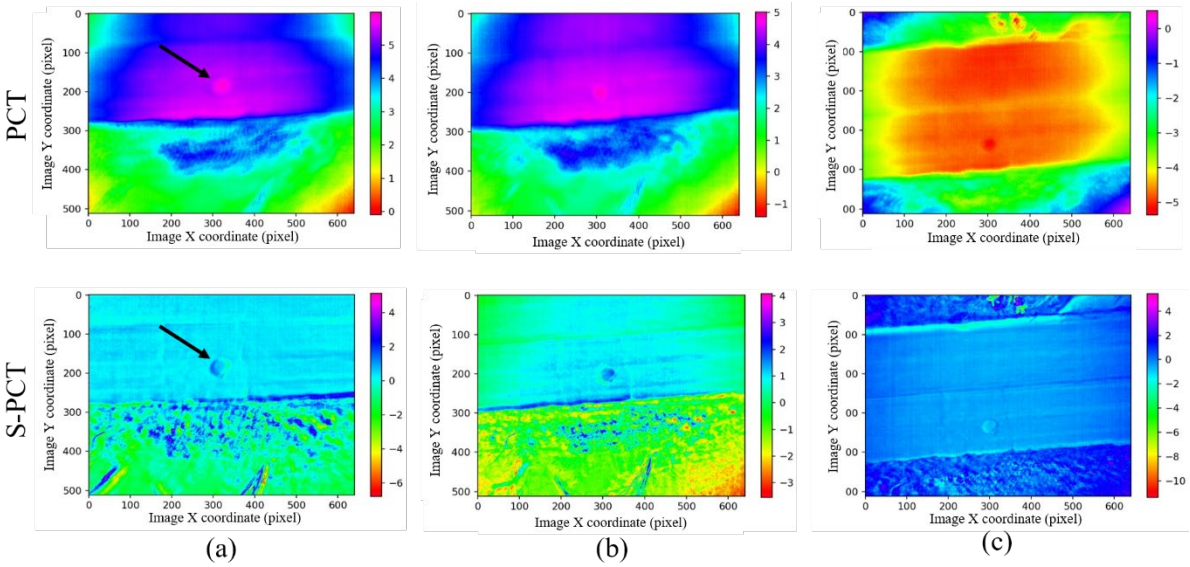

Figure 3.11: PCT and S-PCT for location 1

For tests performed during the second day at location 1, the shadow of a tree was cast on the road surface due to direct sunlight. Because of the shadow, uneven pavement heating occurred in the IR images collected (see Figure 3.12a and Figure 3.12b). Because of the shadow, data cannot be used for identifying subsurface voids because the PCT and S-PCT are sensitive to change in the environment and data produce false-positive results.

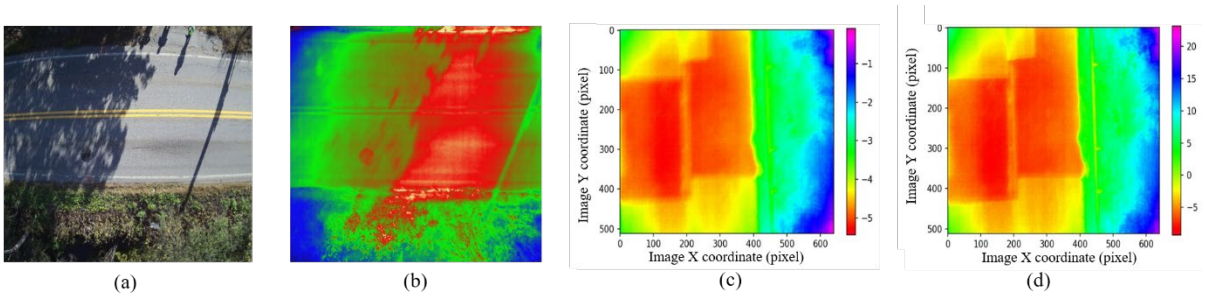

(a) (b) (c) (d)

Figure 3.12: Effect of shadow and no damages

At location 2, no defects were highlighted even when IR images are processed with PCT and S-PCT (see Figure 3.12c and Figure 3.12d). This is a validation of the excellent quality of the maintenance operations performed on the culvert. The only visible discontinuities highlighted by the thermal analysis that are observed in both PCT and S-PCT data are the new layers of asphalt that have been deployed on the roadway.

For the inspection at location 3, the UAV was flown at an altitude of 15 m (50 ft) to optimize the GSD and with cameras in two different orientations, nadiral (i.e., 0 degrees) and 55 degrees. With the IR camera set in nadiral position, the drone must fly over the roadway, which may create a hazard to the traveling traffic. When the IR camera is tilted at an angle, the UAS can hover on the side of the road while collecting images. The goal of this test was to confirm that results are still accurate even when the camera is not perpendicular to the object being tested. The IR images collected every 30 s by hovering the UAS at location 3 on December 1 were processed using PCT (Figure 3.13a) and S-PCT (Figure 3.13b), and the flight details are summarized in Table 3.4.

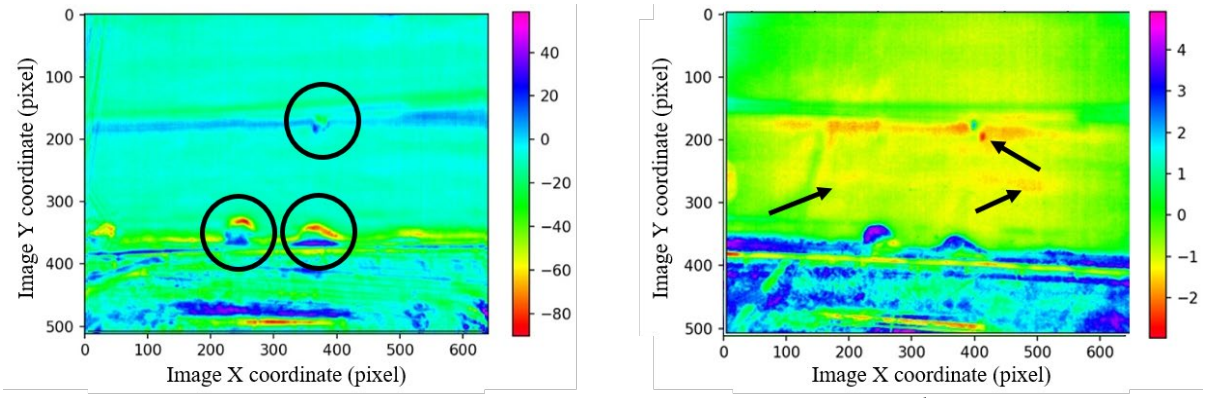

(a) (b)

Figure 3.13: PCT and S-PCT at 0 degrees

Table 3.4: Accuracy with camera in nadiral position

Flight details					
No. of flights (-)	Duration (min)	Sampling rate (s)	Time (hh:mm)	Air temp. (°C)	Water temp. (°C)
1	8.0	30.0	3:00 p.m.	10.0	5

Table 3.5: Accuracy with camera at 55 degrees

Flight details					
No. of flights (-)	Duration (min)	Sampling rate (s)	Time (hh:mm)	Air temp. (°C)	Water temp. (°C)
1	8.0	30.0	3:15 p.m.	10.0	5

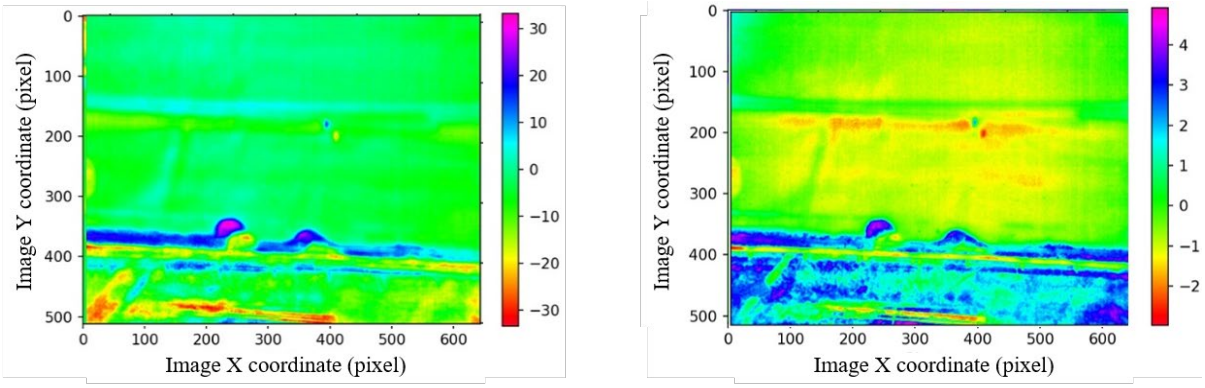

(a) (b)

Figure 3.14: PCT and S-PCT at 55 degrees

As observed from Figure 3.13, both PCT and S-PCT can identify the defects on the roadway's surface represented by the potholes visible in Figure 3.10c and highlighted by circles in Figure 3.13a. When S-PCT is used, additional defects that are not visible in the visible spectrum images and the PCT data can be identified. Those defects are highlighted with arrows in Figure 3.13b. However, for those defects, confirmation from in situ inspections from MassDOT personnel should be required. The same analysis was performed with images collected with the UAS hovering on the side of the road and collecting images with the camera tilted at 55 degrees. The results are shown in Figure 3.14, and the flight details are summarized in Table 3.5. As it is observed from Figure 3.14, no significant differences are highlighted with the images shown in Figure 3.13. It confirms that the camera angle does not affect the detection capability of the system.

Due to features of the UAS such as battery charge and restrictions caused by the road traffic, a time sensitivity analysis is performed to determine the effect of this parameter on the detection accuracy of PCT and S-PCT. The results of the time sensitivity analyses performed

when images are processed using PCT and S-PCT are presented in Figure 3.15 and Figure 3.16, and the flight details are summarized in Table 3.6.

Table 3.6: Accuracy as a function of sampling rate

Flight details					
No. of flights (-)	Duration (min)	Sampling rate (s)	Time (hh:mm)	Air temp. (°C)	Water temp. (°C)
1	30.0	30.0	3:30 p.m.	10.0	5

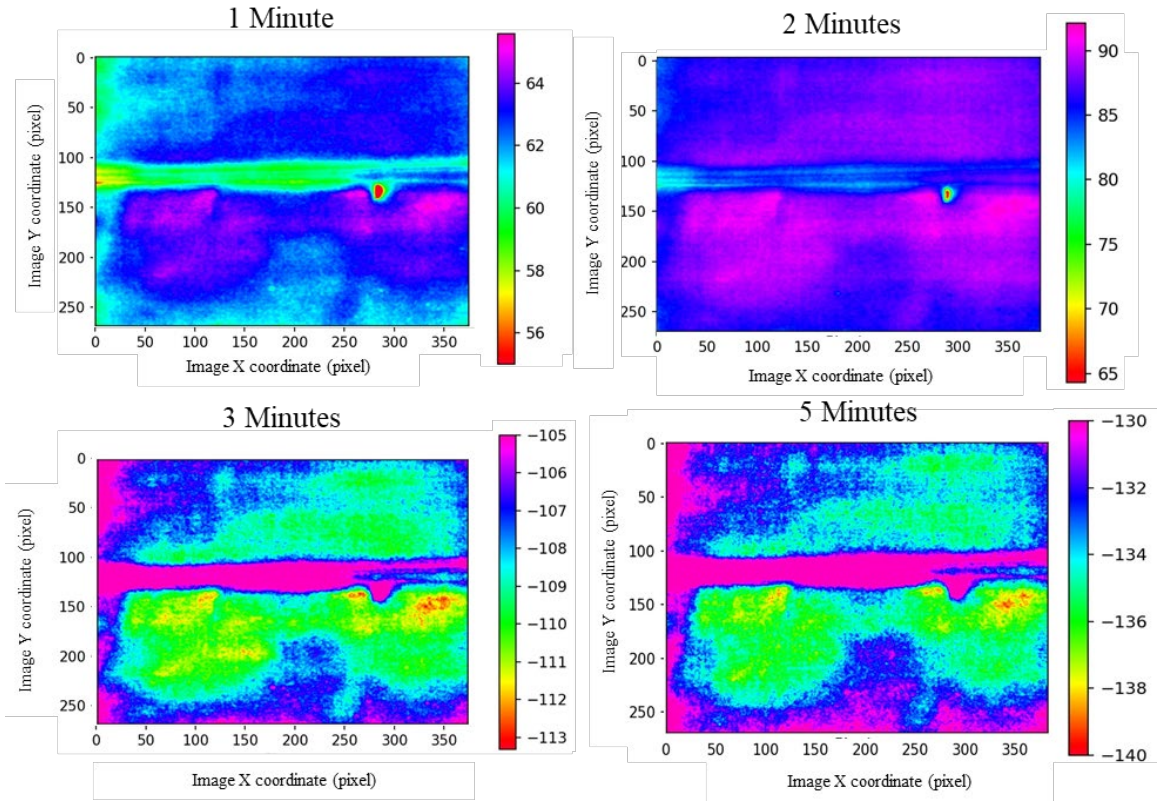

Figure 3.15: Time sensitivity analysis using PCT

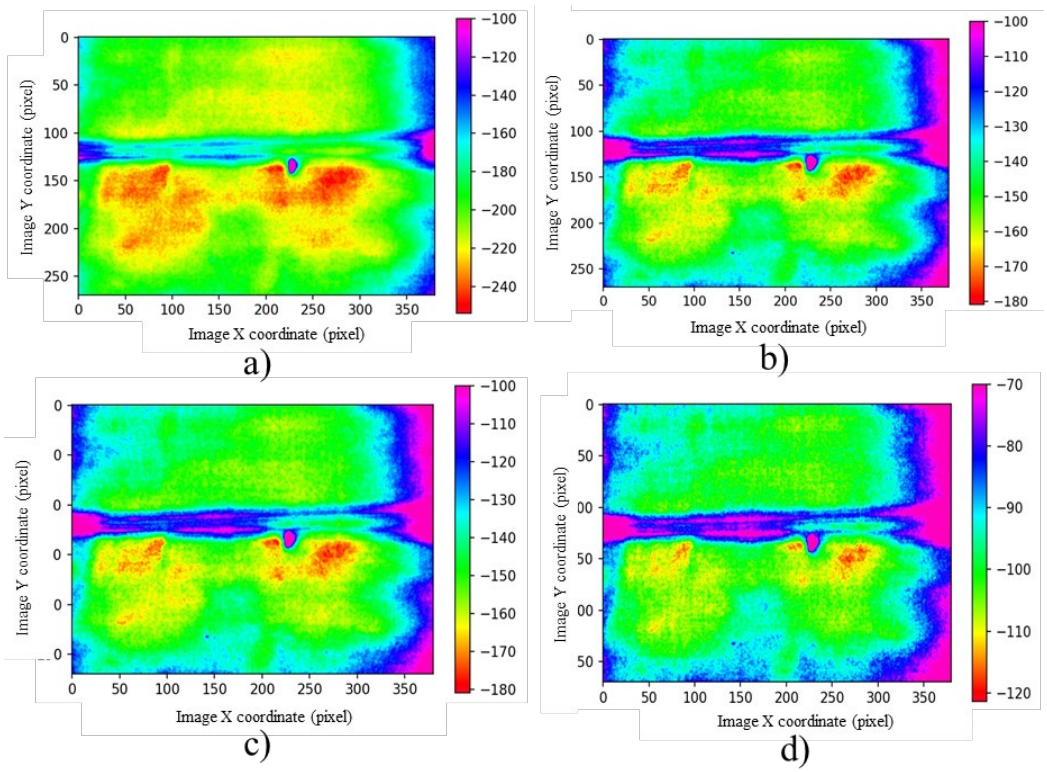

Figure 3.16: Time sensitivity analysis using S-PCT

During the flight, the UAS was kept hovering next to the roadway with the camera in nadiral position for 30 min acquiring IR images every 30 s. A total of 60 IR images was collected for the tests. Data were then decimated to study the effect of the time interval on the accuracy of PCT and S-PCT. For example, 30 images were used for the 1 min scenario, 15 images for the 2 min sampling rate images, and so on for the 3 and 5 min sampling rate considered.

The PCT was found to be sensitive toward the time capturing interval, with increases in the time capturing interval corresponding to reduced performance of the technique. In Figure 3.15, it is observed that as the time capturing interval increases, the quality of the images decreases and the defects start to fade. When a 1 min sampling rate is used, PCT can identify the defects. Because PCT performs linear decomposition, the SNR increases with higher time capturing interval (compare Figure 3.15a to Figure 3.15b). When the same analysis is performed using S-PCT, it is observed that faster sampling rates (i.e., 1 min time capturing interval) allow higher performance. However, results are not very dissimilar when slower sampling rates are considered (see Figure 3.16a–c). As observed in Figure 3.16d, a significant loss of information occurred when the time capturing interval was 5 min. Results suggest that S-PCT is also sensitive toward time capturing interval, but the effect of sampling rate on the accuracy of the results is less pronounced than PCT.

An attempt to perform large-area mapping was made by stitching multiple images to generate an orthomosaic covering an extended portion of the roadway. In this research, a proof of concept was performed using two adjacent IR images. The same principle can be applied to

more images to generate an even larger orthomosaic. During the tests performed, six flights were performed to collect enough temporal data to perform PCT and S-PCT analyses (Table 3.7). The UAS was programmed to collect two IR images with 90% side overlap during each flight. Then each pair of IR images was stitched together using a Speeded Up Robust Feature (SURF) algorithm before performing PCT and S-PCT. An example of the SURF workflow showing the features extraction and matching between two adjacent IR images is shown in Figure 3.17. As observed, two adjacent IR images are considered (Figure 3.17a and Figure 3.17b) and used to determine keypoints (Figure 3.17c). Once the keypoints are matched between the two images, a single larger image composed of the two original ones is obtained (Figure 3.17d and Figure 3.17e). The two original images are indicated by a dashed line and a dashed/dotted line. The process was repeated for all the IR images collected during the six flights, and six stitched images were generated and processed with PCT and S-PCT, obtaining the results shown in Figure 3.18.

Table 3.7: Large-area mapping and orthomosaic generation

Flight details					
No. of flights (-)	Duration (min)	Sampling rate (s)	Time (hh:mm)	Air temp. (°C)	Water temp. (°C)
6	1.0	—	4:30 p.m.	10.0	5

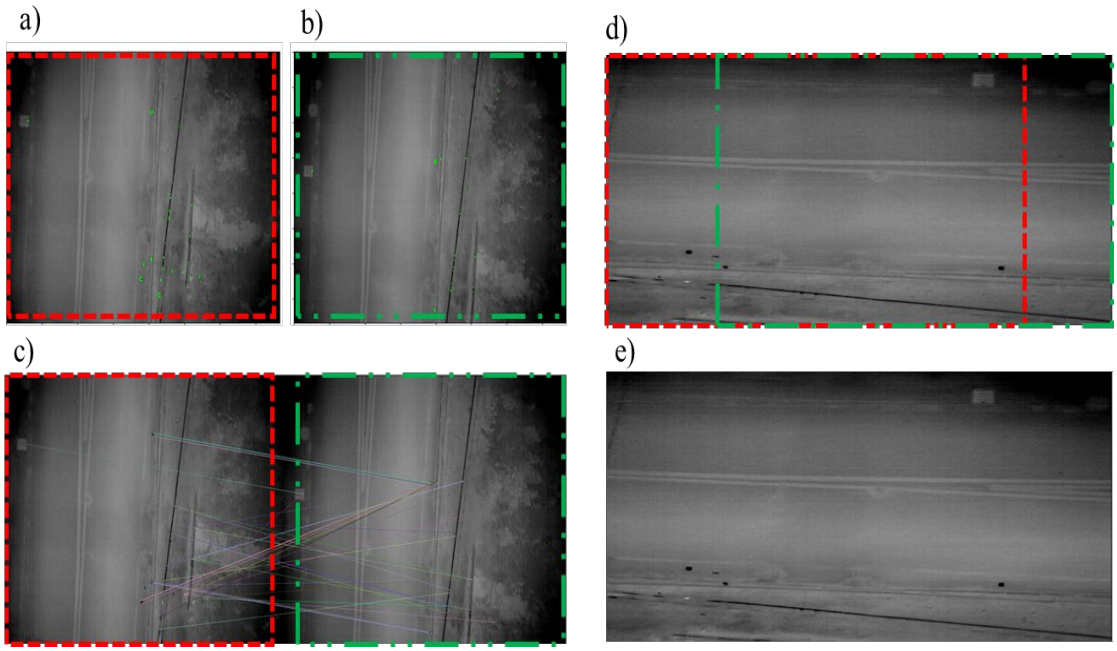

Figure 3.17: SURF algorithm workflow for orthomosaic generation

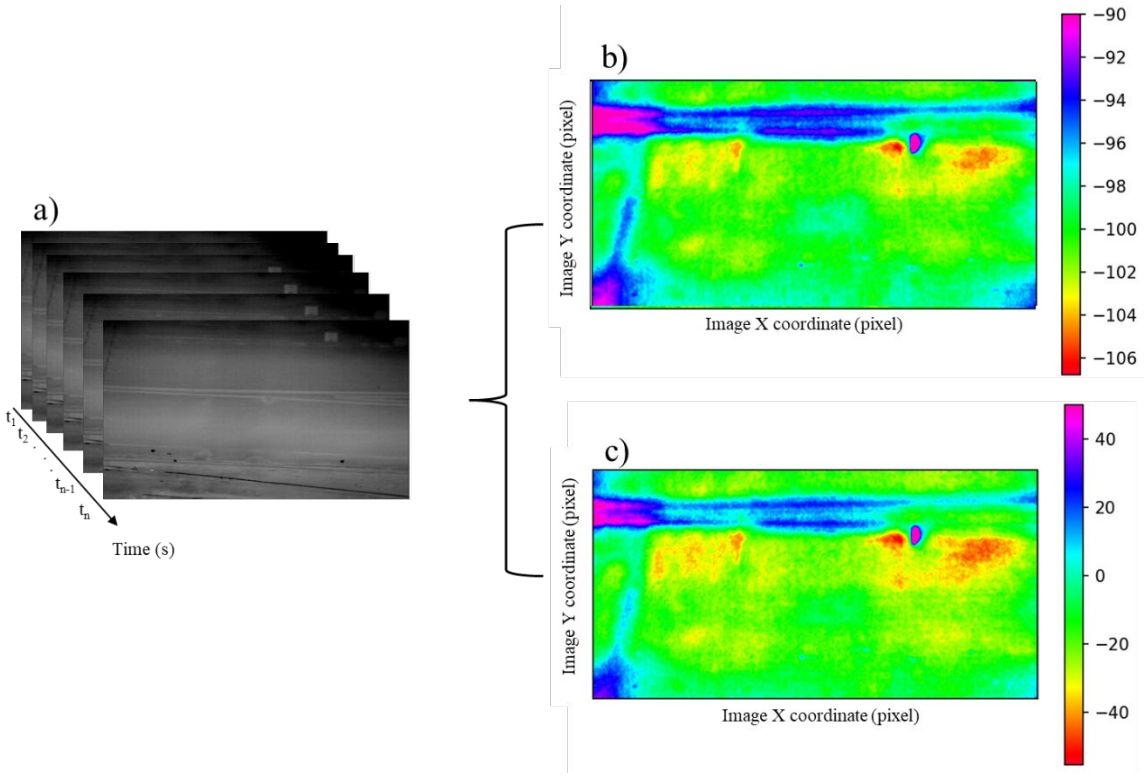

Figure 3.18: Results for large-area mapping

As shown in Figure 3.18, both PCT (Figure 3.18b) and S-PCT (Figure 3.18c) were able to identify the subsurface defects once stitched images (Figure 3.18a) were processed. It can be observed that PCT suffers from some information loss compared to S-PCT. In addition, even if some information loss occurs for the larger area mapping compared to small area mapping (see Figure 3.15a and Figure 3.16a), results are still promising and the defects can be identified clearly. The orthomosaic mapping approach allows mapping a bigger area in a shorter time as a preliminary assessment, and then a more focused analysis can be performed over a smaller area if the defect is seen in the orthomosaic map.

This page was left blank intentionally.

4.0 Best Practices and Conclusions

This study aims to characterize the accuracy of IRT combined with UASs to be used as a technique for detecting voids underneath roadways that can represent failing culverts and underground structures. Subsurface voids caused by erosion of materials through cracks in culverts or drainage pipes are the first signs of damaged infrastructure. If not detected in time, subsurface voids can propagate underneath the pavement surface and cause sinkholes and the collapse of the roadway. For this reason, novel NDE approaches that can simplify the inspection process and provide information about the location and severity of the defects are sought. The work performed in this feasibility study focuses on the experimental validation UAS-AIR_T for detecting soil voids and assessing the conditions of underground structures. Extensive laboratory and field tests have been performed to determine the system's accuracy as a function of different working conditions such as the type of IRT method used, IR camera angle, and image post-processing technique used. Laboratory tests were performed on a mock roadway that replicated the structure of highway pavement in Massachusetts. The mock roadway was damaged by extracting a known volume of soil from its subbase to create voids having increasing size. The outdoor validations were performed on three in-service culverts with different levels of damage.

The laboratory tests showed that when traditional IR processing methods such as first and second derivatives were used, IRT could not detect subsurface voids. For this reason, more advanced image processing techniques such as R^2-based analysis, PCT, and S-PCT were used. In particular, the R^2-based analysis was able to detect the larger defects but results were inconsistent. PCT and S-PCT demonstrated superior performances even if PCT was only able to locate the smaller defects. S-PCT was able to locate the defects in all the analyzed scenarios with an average accuracy of ~80% when the dimension of the damage in the IR images is compared to the surface of the actual defect. The detection accuracy of the three methods was also checked as a function of the sampling rate used to capture the IR images. The results demonstrated that the PCT was sensitive toward the image-capturing interval and that a slower sampling rate decreases the method's accuracy. To overcome this issue, a mixed time interval was proposed and the detection accuracy of PCT increased by ~13%. S-PCT was a more robust method and accuracy error was below 5% for IR images captured every 2 min as the road surface was cooling down. On average, S-PCT has shown an error of 11% depending on the sampling interval used.

PCT and S-PCT methods were used for outdoor testing due to their better performance in the indoor setting. The IR images were collected with a UAS hovering at different altitudes to show how defect size is a function of the GSD. During the field tests, PCT and S-PCT were able to detect defects in the soil that have progressed and reached the roadway's surface forming potholes. S-PCT also seems capable of detecting voids underneath the road's surface that are not yet causing damage to the pavement. However, further investigations must be performed to confirm the location and severity of those damages. Overall, field tests confirmed the results of the laboratory experiments and provided some insight into best practices that should be implemented during future real-world operations, as summarized by the following:

- The accuracy of IRT can be enhanced by using S-PCT as an image post-processing technique. An image's first and second derivatives do not provide information about subsurface defects.

- The presence of water on the road's surface (e.g., after heavy rain) makes it challenging to detect subsurface voids. A different thermal emissivity characterizes the water compared to the pavement, resulting in spots in the IR image that can be confused as defects. Therefore, the IR inspection should be performed when pavements are dry and have not received rain for a few days.

- Shadows and direct sunlight cause the IRT to be ineffective. Inspections should be performed at night or during overcast days to reduce the effects of direct sun irradiation. The presence of shadow increases the possibility of a false positive.

- Inspection should be performed when the roadway starts to emit thermal energy after being heated for an extended time by the sun to maximize the thermal gradient with the environment. For this reason, dusk or night inspections should be preferred.

- A water–road surface temperature differential above 10°C (from the historical data) should theoretically provide more accurate results and identify subsurface defects. However, because inspections were performed between November and December only, no conclusions can be made about the optimal time of the year when the inspection should be performed.

- Flying the UAS at a lower altitude allows for a better GSD and pixel resolution. Because of the size of subsurface voids in real-world applications, not much difference is observed when flying at 15 m (50 ft) altitude compared to 21 m (70 ft) altitude. However, operating the UAS at a lower altitude should be preferred when possible.

- The approach in which the UAS hovers above the inspected culvert and collects data every 30 s for 8 min allows identifying subsurface defects and provides enough data that can be decimated if needed. A more extended image collection period (i.e., 30 min) can also be used, but the improved accuracy does not justify the extended time spent flying the UAS in a single position.

- IR images should be collected with a sampling rate that depends on the roadway's cooling rate. During the steepest part of the cooling curve, IR images can be collected at a faster sampling rate, then the acquisition time may be decreased once the road surface reaches thermal equilibrium with the surrounding environment.

- For IR orthomosaics of larger areas, images must be collected with a 90% side overlap to allow enough keypoints in subsequent images to be recognized. With lower side overlaps, the SURF algorithm may not recognize enough features in adjacent views of the targeted portion of the road, making it impossible to stitch images.

- Flying the UAS nadiral to the road surface (i.e., camera at a 0-degree angle) or on the side (i.e., camera at a 55-degree angle) provides similar results. The possibility of collecting nadiral or oblique flights should be decided based on the type of road, characteristics of the surroundings (e.g., trees or power lines), and drone specifications that allow or do not allow the UAS to fly above live traffic.

- Flying the UAS back-and-forth between locations to be inspected can be done only if the time between two subsequent flights at the same location is below 10 min. Because the accuracy of PCT and S-PCT is a function of the sampling rate, damage detection capabilities decrease significantly for a sampling rate slower than 10 min.

Finally, future research directions are provided to advance the use of UAS-AIR_T and allow the field deployment of this technology. Particular attention should be given to the following:

- Understanding the effect of a temperature differential between the road surface and the water. Studies that consider a year-long period should be performed to validate the accuracy of PCT and S-PCT for different temperatures and to identify the optimal time(s) of the year for the inspection.

- Assessing the possibility to use machine learning methods such as convolutional neural networks and image segmentation algorithms for autonomous damage identification and narrowing down the portion of the roadway that presents subsurface voids.

- The possibility of advancing UAS-AIR_T for inspecting other infrastructure systems (e.g., bridges) in addition to roadways and identifying subsurface voids that can eventually result in structural failures.

5.0 References

1. Virginia Department of Transportation. Potholes. https://www.virginiadot.org/info/faq-potholes.asp. Accessed Nov. 2021.
2. Tharp, T. M. Mechanics of Upward Propagation of Cover-Collapse Sinkholes. *Engineering Geology*, Vol. 52, No. 1–2, 1999, pp. 23–33.
3. Strauch, J. A. From Tiny Hole to Huge Problem Overnight—Emergency Culvert Pipe Repair. In *Pipelines 2012: Innovations in Design, Construction, Operations, and Maintenance, Doing More with Less,* Reston, VA: ASCE, 2012, pp. 682–690.
4. Perrin, J. Jr., C. S. Jhaveri, and J. Perrin Jr. The Economic Costs of Culvert Failures, Prepared for TRB 2004 Annual Meeting, Washington, D.C., 2004.
5. McInnes, S., and J. Quirus. Plymouth Road over Plymouth Creek: The Sinkhole That Stopped Traffic. In *67th Highway Geology Symposium*, 2016.
6. ASCE. Report Card for America's Infrastructure. Reston, VA: ASCE, 2021. https://infrastructurereportcard.org/. Accessed Nov. 2021.
7. Minnesota Department of Transportation. Maintenance Culvert Cost Data Analysis. Jan. 12, 2015. http://www.dot.state.mn.us/bridge/hydraulics/culvertcost/2015%20Drainage%20Maintenance%20Data%20Summary%20-%20Final%20Version.pdf. Accessed November 2021.
8. Rizzo, R. J., and L. S. Bryson. Remote Sensing Application for Sinkhole Monitoring along Roadways. *SoutheastCon*, Vol. 2, 2020, pp. 1–2.
9. Najafi, M., and D. V. Bhattachar. Development of a Culvert Inventory and Inspection Framework for Asset Management of Road Structures, *Journal of King Saud University-Science,* Vol. 23, No. 3, 2011, pp. 243–254.
10. Piratla, K. R., W. Pang, H. Jin, and M. Stoner. Best Practices for Assessing Culvert Health and Determining Appropriate Rehabilitation Methods. Final Report, South Carolina Department of Transportation, 2017.
11. Robot, L., I. Manyoe, Y. Arifin, M. Saputra, A. Bilgais, R. Abdullah, and S. Napu. Surface and Subsurface Analysis Based on the Geological Structure and Electrical Resistivity Data in Gorontalo Outer Ring Road (GORR), Huidu Utara. *Journal of Physics: Conference Series* , Vol. 1968, No. 1, 2021, p. 012054.
12. Fang, Z., Z. Shi, and J. Liu. Subsurface Space Investigation Jointly Using Seismic Reflection and Refraction Tomography in Urban Area: A Case Study of Hangzhou, China. *IOP Conference Series: Earth and Environmental Science*, Vol. 660, No. 1, 2021, p. 012007.
13. Li, H. (2021). Research on Technology and Application of Buried Faults Identification in Urban Underground Space. *CONVERTER*, 848–860. https://doi.org/10.17762/converter.350. Accessed Nov. 2021.
14. Applied Research Associates, Inc. Detection and Mitigation of Subsidence Voids on Vermont Roadways. Final Report, Vermont Agency of Transportation, May 30, 2008. https://vtrans.vermont.gov/sites/aot/files/highway/documents/materialsandresearch/completedprojects/AOT-ARARoadSubsidenceFinalRpt.pdf. Accessed November 2021).

15. Benedetto, A., F. Tosti, L. B. Ciampoli, and F. D'Amico. An Overview of Ground-Penetrating Radar Signal Processing Techniques for Road Inspections. *Signal Processing*, Vol. 132, Mar. 2017, pp. 201–209.
16. Solla, M., V. Pérez-Gracia, and S. J. R. S. Fontul. A Review of GPR Application on Transport Infrastructures: Troubleshooting and Best Practices. *Remote Sensing,* Vol. 13, No. 4, 2021, p. 672.
17. Joshaghani, A., and M. Shokrabadi. Ground Penetrating Radar (GPR) Applications in Concrete Pavements. *International Journal of Pavement Engineering*, 2021, pp. 1–28. https://doi.org/10.1080/10298436.2021.1954182.
18. Friedt, J. M., G. Martin, G. Goavec-Mérou, D. Rabus, S. Alzuaga, L. Arapan, M. Sagnard, and É. Carry. Acoustic Transducers as Passive Cooperative Targets for Wireless Sensing of the Sub-Surface World: Challenges of Probing with Ground Penetrating RADAR. *Sensors*, Vol. 18, No. 1, 2018, p. 246.
19. Bianchini Ciampoli, L., F. Tosti, N. Economou, and F. Benedetto. Signal Processing of GPR Data for Road Surveys. *Geosciences*, Vol. 9, No. 2, 2019, p. 96.
20. Tosti, F., V. Gagliardi, F. D'Amico, and A. M. Alani. Transport infrastructure monitoring by data fusion of GPR and SAR imagery information. *Transportation Research Procedia*, Vol. 45, 2020, pp. 771–778.
21. Klotzsche, A., H. Vereecken, and J. van der Kruk. Review of Crosshole Ground-Penetrating Radar Full-Waveform Inversion of Experimental Data: Recent Developments, Challenges, and Pitfalls. *Geophysics*, Vol. 84, No. 6, 2019, pp. H13–H28.
22. Rhee, J. Y., K. T. Park, J. W. Cho, and S. Y. Lee. A Study of the Application and the Limitations of Gpr Investigation on Underground Survey of the Korean Expressways. *Remote Sensing*, Vol. 13, No. 9, 2021, p. 1805.
23. Miura, H., A. Watanabe, M. Okugawa, and T. Miura. Verification and Evaluation of Robotic Inspection of the Inside of Culvert Pipes. *Journal of Robotics and Mechatronics*, Vol. 31, No. 6, 2019, pp. 794–802.
24. Meegoda, J. N., J. A. Kewalramani, and A. Saravanan. Adapting 360-Degree Cameras for Culvert Inspection: Case Study. *Journal of Pipeline Systems Engineering and Practice*, Vol. 10, No. 1, 2019, 05018005.
25. Youngblood, D., and C. D. M Smith. Enhanced Culvert Inspections Best Practices Guidebook. *Minnesota Dept. of Transportation*, *Research Services and Library*, Rept. No. MN/RC 2017-16, June 2017.
26. Kalhor, D., S. Ebrahimi, R. B. Tokime, F. A. Mamoudan, Y. Bélanger, A. Mercier, and X. Maldague. Cavity Detection in Steel-Pipe Culverts using Infrared Thermography. *Applied Sciences*, Vol. 11, No. 9, 2021, p. 4051.
27. Meola, C. Origin and Theory of Infrared Thermography, in *Infrared Thermography Recent Advances and Future Trends*, Bentham eBooks, 2012, pp. 3–28.
28. Vyas, V., V. J. Patil, A. P. Singh, and A. Srivastava. Application of Infrared Thermography for Debonding Detection in Asphalt Pavements. *Journal of Civil Structural Health Monitoring*, Vol. 9, No. 3, 2019, pp. 325–337.
29. Washer, G., R. Fenwick, and N. Bolleni. Effects of Solar Loading on Infrared Imaging of Subsurface Features in Concrete. *Journal of Bridge Engineering*, Vol. 15, No. 4, 2010, pp. 384–390.

30. Sham, J. F., S. A. Memon, and Y. Lo. Application of Continuous Surface Temperature Monitoring Technique for Investigation of Nocturnal Sensible Heat Release Characteristics by Building Fabrics in Hong Kong. *Energy and Buildings*, Vol. 58, 2013, pp. 1–10.
31. Sham, J. F., T. Y. Lo, S. A. Memon. Verification and Application of Continuous Surface Temperature Monitoring Technique for Investigation of Nocturnal Sensible Heat Release Characteristics by Building Fabrics. *Energy and Buildings*, Vol. 53, 2012, pp. 108–116.
32. Janků, M., I. Březina, and J. Grošek. Use of Infrared Thermography to Detect Defects on Concrete Bridges. *Procedia Engineering*, Vol. 190, 2017, pp. 62–69.
33. Maldagure, X. P. *Theory and Practice of Infrared Technology for Nondestructive Testing*. John Wiley & Sons, New York, 2001.
34. Maldague, X., and S. Marinetti. Pulse Phase Infrared Thermography. *Journal of Applied Physics*, Vol. 79, No. 5, 1996, pp. 2694–2698.
35. Chatterjee, K., S. Tuli, S. G. Pickering, and D. P. Almond. A Comparison of the Pulsed, Lock-In and Frequency Modulated Thermography Nondestructive Evaluation Techniques. *NDT & E International*, Vol. 44, No. 7, 2011, pp. 655–667.
36. Wiecek, B. Review on Thermal Image Processing for Passive and Active Thermography, in 2005 *IEEE Engineering in Medicine and Biology 27th Annual Conf.*, 2006, pp. 686–689.
37. Hiasa, S., R. Birgul, M. Matsumoto, and F. N. Catbas. Experimental and Numerical Studies for Suitable Infrared Thermography Implementation on Concrete Bridge Decks. *Measurement*, Vol. 121, 2018, pp. 144–159.
38. Wang, G., P. W. Tse, and M. Yuan. Automatic Internal Crack Detection from a Sequence of Infrared Images with a Triple-Threshold Canny Edge Detector. Vol. 29, No. 2, 2018, p. 25403.
39. Montaggioli, G., M. Puliti, and A. Sabato. Automated Damage Detection of Bridge's Sub-Surface Defects from Infrared Images Using Machine Learning, in *Health Monitoring of Structural and Biological Systems XV*, International Society for Optics and Photonics, SPIE, Bellingham, WA, Vol. 11593, May 6, 2021, p. 115932A.
40. Lucchi, E. Applications of the Infrared Thermography in the Energy Audit of Buildings: A Review. *Renewable and Sustainable Energy Reviews*, Vol. 82, 2018, pp. 3077–3090.
41. Barreira, E., R. M. Almeida, and M. L. Simões. Emissivity of Building Materials for Infrared Measurements, *Sensors*, Vol. 21, No. 6, 2021, p. 1961.
42. Balaras, C. A., and A. A. Argiriou. Infrared thermography for building diagnostics, *Energy and Buildings*, Vol. 34, 2002, pp. 171–183.
43. Puliti, M., G. Montaggioli, and A. Sabato. Automated Subsurface Defects' Detection Using Point Cloud Reconstruction from Infrared Images. *Automation in Construction*, Vol. 129, 2021, p. 103829.
44. Sabato, A., M. Puliti, and C. Niezrecki. Combined Infrared Imaging and Structure from Motion Approach for Building Thermal Energy Efficiency and Damage Assessment, in *Proc., SPIE, Health Monitoring of Structural and Biological Systems XIV*, Vol. 11381, Apr. 22, 2020, p. 1138125.

45. Doshvarpassand, S., C. Wu, and X. Wang. An Overview of Corrosion Defect Characterization Using Active Infrared Thermography. *Infrared Physics & Technology*, 96, Jan. 2019, pp. 366–389.
46. Meola, C., S. Boccardi, and G. M. Carlomagno. *Infrared Thermography in the Evaluation of Aerospace Composite Materials: Infrared Thermography To Composites*. Woodhead Publishing, Amsterdam, 2016.
47. Duan, Y., P. Servais, M. Genest, C. Ibarra-Castanedo, and X. P. Maldague. ThermoPoD: A Reliability Study on Active Infrared Thermography for the Inspection of Composite Materials. *Journal of Mechanical Science Technology*, Vol. 26, No. 7, 2012, pp. 1985–1991.
48. Boccardi, S., N. Boffa, G. Carlomagno, L. Maio, C. Meola, and F. Ricci. Infrared Thermography and Ultrasonics to Evaluate Composite Materials for Aeronautical Applications. *Journal of Physics: Conference Series*, Vol. 658, No. 1, 2015, p. 012007.
49. Garrido, I., S. Lagüela, and P. Arias. Infrared Thermography's Application to Infrastructure Inspections. *Infrastructures*, Vol. 3, No. 3, 2018, p. 35.
50. S. Abu Dabous, and S. Feroz. Condition Monitoring of Bridges with Non-Contact Testing Technologies. *Automation in Construction*, Vol. 116, Aug. 2020, 103224.
51. Sanati, H., D. Wood, and Q. Sun. Condition Monitoring of Wind Turbine Blades Using Active and Passive Thermography. *Applied Sciences*, Vol. 8, No. 10, 2018, 2004.
52. López, F., S. Sfarra, A. Chulkov, C. Ibarra-Castanedo, H. Zhang, M. A. Omar, V. Vavilov, and X. P. V. Maldague. Thermal Stresses Applied on Helicopter Blades Useful to Retrieve Defects by Means of Infrared Thermography and Speckle Patterns. *Thermal Science and Engineering Progress*, Vol. 18, 2020, 100511.
53. Bagavathiappan, S., B. Lahiri, T. Saravanan, J. Philip, and T. Jayakumar. Infrared Thermography for Condition Monitoring–A Review. *Infrared Physics Technology,* Vol. 60, Sept. 2013, pp. 35–55.
54. Büyüköztürk, O. Imaging of Concrete Structures. *NDT & E International*, Vol. 31, No. 4, 1998, pp. 233–243.
55. Rocha, J. H. A., C. F. Santos, and Y. V. Póvoas. Evaluation of the Infrared Thermography Technique for Capillarity Moisture Detection in Buildings. *Procedia Structural Integrity*, Vol. 11, 2018, pp. 107–113.
56. Aquino Rocha, J. H., and Y. Vieira Póvoas Tavares. Infrared Thermography as a Non-Destructive Test for the Inspection of Reinforced Concrete Bridges: A Review of the State of the Art. *Revista ALCONPAT*, Vol. 7, No. 3, 2017, pp. 200–214.
57. Kashif Ur Rehman, S., Z. Ibrahim, S. A. Memon, and M. Jameel. Nondestructive Test Methods for Concrete Bridges: A Review. *Construction and Building Materials*, Vol. 107, Mar. 15, 2016, pp. 58–86.
58. Omar, T., M. L. Nehdi, and T. Zayed. Infrared Thermography Model for Automated Detection of Delamination in RC Bridge Decks. *Construction and Building Materials*, Vol. 168, 2018, pp. 313–327.
59. Ali, R., and Y. J. Cha. Subsurface Damage Detection of a Steel Bridge Using Deep Learning and Uncooled Micro-Bolometer. *Construction and Building Materials*, Vol. 226, 2019, pp. 376–387.
60. Anchuela, Ó. P., P. Frongia, F. Di Gregorio, A. C. Sainz, and A. P. Juan. Internal characterization of embankment dams using ground penetrating radar (GPR) and

thermographic analysis: A case study of the Medau Zirimilis Dam (Sardinia, Italy). *Engineering Geology*, Vol. 237, 2018, pp. 129–139.
61. Sim, J.-G. Improved Image Processing of Road Pavement Defect by Infrared Thermography. *Selected Scientific Papers—Journal of Civil Engineering,* Vol. 13, No. s1, 2018, pp. 61–72.
62. Bach, P. M., and J. K. Kodikara. Reliability of Infrared Thermography in Detecting Leaks in Buried Water Reticulation Pipes. *IEEE Journal of Select Topics in Applied Earth Observations and Remote Sensing*, Vol. 10, No. 9, 2017, pp. 4210–4224.
63. Kalhor, D., S. Ebrahimi, R.B. Tokime, F.A. Mamoudan, Y. Bélanger, A. Mercier, and X. Maldague. Infrared Thermography for Culvert Inspection. *3rd Int. Symp. on Structural Health Monitoring and Nondestructive Testing*, Nov. 25–26, 2020, Quebec City, Quebec, Canada.
64. Niezrecki, C., J. Baqersad, and A. Sabato. Digital Image Correlation Techniques for NDE and SHM, in *Handbook of Advanced Nondestructive Evaluation*, N. Ida and N. Meyendorf, eds. Cham, Switzerland: Springer International Publishing, 2019, pp. 1545–1590.
65. Khaloo, A., D. Lattanzi, A. Jachimowicz, and C. Devaney. Utilizing UAV and 3D Computer Vision for Visual Inspection of a Large Gravity Dam. *Frontiers in Built Environment*, Vol. 4, July 2, 2018, pp. 1–16.
66. Reagan, D., A. Sabato, and C. Niezrecki. Feasibility of Using Digital Image Correlation for Unmanned Aerial Vehicle Structural Health Monitoring of Bridges. *Structural Health Monitoring*, Vol. 17, No. 5, 2018, pp. 1056–1072.
67. Khaloo, A., and D. Lattanzi. A Hierarchical Computer Vision Approach to Infrastructure Inspection, in *2015 Int. Workshop on Computing in Civil Engineering, Proceedings*, January 2015, pp. 540–547.
68. Hallermann, N., G. Morgenthal, and V. Rodehorst. Unmanned Aerial Systems (UAS)—Case Studies of Vision Based Monitoring of Ageing Structures, in *Int. Symp. Non-Destructive Test. Civ. Eng.*, Berlin, Proceedings Vol. 20, No. 11, 2015, pp. 1–10.
69. Liu, Y. F., X. G. Liu, J. S. Fan, B. F. Spencer Jr, X. C. Wei, S. Y. Kong, and X. H. Guo. Refined Safety Assessment of Steel Grid Structures with Crooked Tubular Members. *Automation in Construction*, Vol. 99, Mar. 2019, pp. 249–264.
70. Jafari, B., A. Khaloo, and D. Lattanzi. Deformation Tracking in 3D Point Clouds Via Statistical Sampling of Direct Cloud-to-Cloud Distances. *Journal of Nondestructive Evaluation*, Vol. 36, No. 4, 2017, pp. 1–10.
71. Kerle, N., F. Nex, M. Gerke, D. Duarte, and A. Vetrivel. UAV-Based Structural Damage Mapping: A Review. *ISPRS International Journal of Geo-Information*, Vol. 9, No. 1, (2020), 14.
72. Wang, X., C. E. Wittich, T. C. Hutchinson, Yehuda Bock, Dara Goldberg, Eric Lo, and F. Kuester. Methodology and Validation of UAV-Based Video Analysis Approach for Tracking Earthquake-Induced Building Displacements. *Journal of Computing in Civil Engineering*, Vol. 34, No. 6, 2020, 04020045.
73. Bhowmick, S., S. Nagarajaiah, and A. Veeraraghavan. Vision and Deep Learning-Based Algorithms to Detect and Quantify Cracks on Concrete Surfaces from UAV Videos. *Sensors*, Vol. 20, No. 21, 2020, 6299.

74. Kim, H., J. Lee, E. Ahn, S. Cho, M. Shin, and S.-H. Sim. Concrete Crack Identification Using a UAV Incorporating Hybrid Image Processing, *Sensors*, Vol. 17, No. 9, 2017, 2052.
75. Hiasa, S., F. Necati Catbas, M. Matsumoto, and K. Mitani. Considerations and Issues in the Utilization Of Infrared Thermography for Concrete Bridge Inspection at Normal Driving Speeds. *Journal of Bridge Engineering*, Vol. 22, No. 11, 2017, 04017101.
76. Omar, T., and M. L. Nehdi. Remote Sensing of Concrete Bridge Decks Using Unmanned Aerial Vehicle Infrared Thermography. *Automation in Construction*, 83, Nov. 2017, 360–371.
77. U.S. Geological Survey. USGS Water Data for Massachusetts. https://waterdata.usgs.gov/ma/nwis/nwis. Accessed Dec. 2020.
78. NOAA. Road Weather Information System (RWIS) Data. https://madis.ncep.noaa.gov/madis_rwis.shtml. Accessed Mar. 2021.
79. Massachusetts Highway Department. Project Development & Design Guide, 2006. https://www.mass.gov/doc/2006-project-development-and-design-guide/download.
80. Teledyne. Dual Payload Drone Gimbal FLIR XT2, 2021, https://www.flir.com/products/xt2/. Accessed Nov. 2021.
81. DJI. Matrice 200 Series V2. https://www.dji.com/matrice-200-series-v2. Accessed Nov. 2021.
82. Federal Aviation Administration. Certificated Remote Pilots Including Commercial Operators: Part 107. https://www.faa.gov/uas/commercial_operators/. Accessed Nov. 2021.
83. Lu, R., X. Yang, W. Li, J. Fan, D. Li, and X. Jing. Robust Infrared Small Target Detection Via Multidirectional Derivative-Based Weighted Contrast Measure. *IEEE Geoscience and Remote Sensing Letters*, Vol. 19, Oct. 2020, 7000105.
84. Qu, Z., P. Jiang, and W. Zhang. Development and Application of Infrared Thermography Non-Destructive Testing Techniques. *Sensors*, Vol. 20, No. 14, 2020, 3851.
85. Wang, Q., R. Xia, Q. Liu, H. Zhou, J. Qiu, and B. Zhao. Pixel-Based Thermal Sequence Processing Algorithm Based on R^2 Fractile Threshold of Non-Linear Fitting in Active Infrared Thermography. *Infrared Physics Technology*, Vol. 109, 2020, p. 103422.
86. Wold, S., K. Esbensen, and P. Geladi. Principal Component Analysis. *Chemometrics and Intelligent Laboratory Systems*, Vol. 2, No. 1–3, 1987, pp. 37–52.
87. Wall, M. E., A. Rechtsteiner, and L. M. Rocha. Singular Value Decomposition and Principal Component Analysis, in *A Practical Approach to Microarray Data Analysis*: Springer, Boston. 2003, pp. 91–109.
88. Rajic, N. Principal Component Thermography for Flaw Contrast Enhancement and Flaw Depth Characterisation in Composite Structures. *Composite Structures*, Vol. 58, No. 4, 2002, pp. 521–528.
89. Milovanović, B., M. Gaši, and S. Gumbarević. Principal Component Thermography for Defect Detection in Concrete. *Sensors*, Vol. 20, No. 14, 2020, p. 3891.
90. Yousefi, B., S. Sfarra, C. I. Castanedo, and X. P. Maldague. Thermal NDT Applying Candid Covariance-Free Incremental Principal Component Thermography (CCIPCT), in *Thermosense: Thermal Infrared Applications XXXIX*, Proceedings Vol. 10214, 2017, p. 102141I.

91. Yousefi, B., C. Ibarra-Castanedo, and X. P. Maldague. Infrared Non-Destructive Testing via Semi-Nonnegative Matrix Factorization, in *15th Int. Workshop on Advanced Infrared Technology and Applications*, Proceedings, Vol. 27, No. 1, 2019, p. 13.
92. Zou, H., T. Hastie, and R. Tibshirani. Sparse Principal Component Analysis. *Journal of Computational Graphical Statistics*, Vol. 15, No. 2, 2006, pp. 265–286.
93. Jenatton, R., G. Obozinski, and F. Bach. Structured sparse principal component analysis, in *13th Int. Conf. on Artificial Intelligence and Statistics*, Proceedings, 2010, pp. 366–373.
94. d'Aspremont, A., F. Bach, and L. El Ghaoui. Optimal Solutions for Sparse Principal Component Analysis. *Journal of Machine Learning Research*, Vol. 9, No. 7, (2008), pp. 1269–1294.
95. Parvataneni, R. Principal Component Thermography for Steady Thermal Perturbation Scenarios. MS thesis, 2009, Clemson Univ.
96. Wen, C.-M., S. Sfarra, G. Gargiulo, and Y. Yao. Thermographic Data Analysis for Defect Detection by Imposing Spatial Connectivity and Sparsity Constraints in Principal Component Thermography. *IEEE Transactions on Industrial Informatics,* Vol. 17, No. 6, 2020, pp. 3901–3909.
97. Yousefi, B., S. Sfarra, C. I. Castanedo, and X. P. Maldague. Comparative Analysis on Thermal Non-Destructive Testing Imagery Applying Candid Covariance-Free Incremental Principal Component Thermography (CCIPCT). *Infrared Physics Technology*, Vol. 85, 2017, pp. 163–169.
98. Wu, J.-Y., S. Sfarra, and Y. Yao. Sparse Principal Component Thermography for Structural Health Monitoring of Composite Structures. *IFAC-PapersOnLine*, Vol. 51, No. 24, 2018, pp. 855–860.

6.0 Appendices

6.1 Appendix A: Historical water and road temperature data

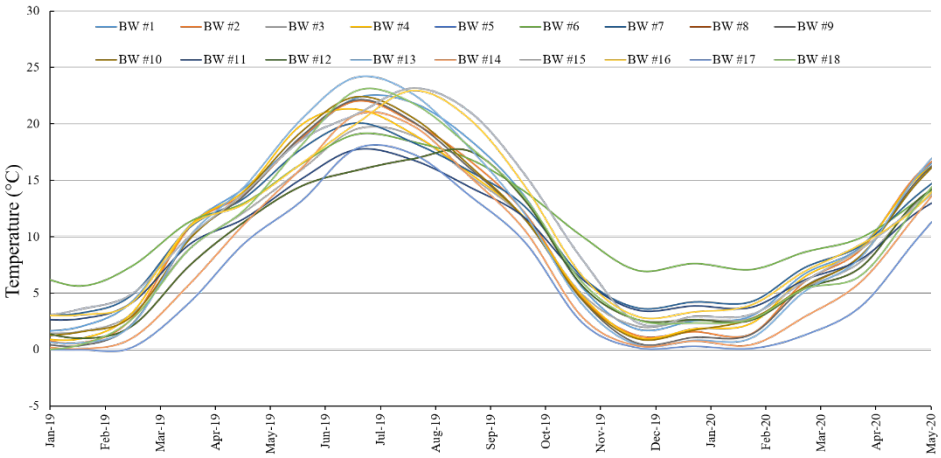

Figure A.1: Water temperature by month

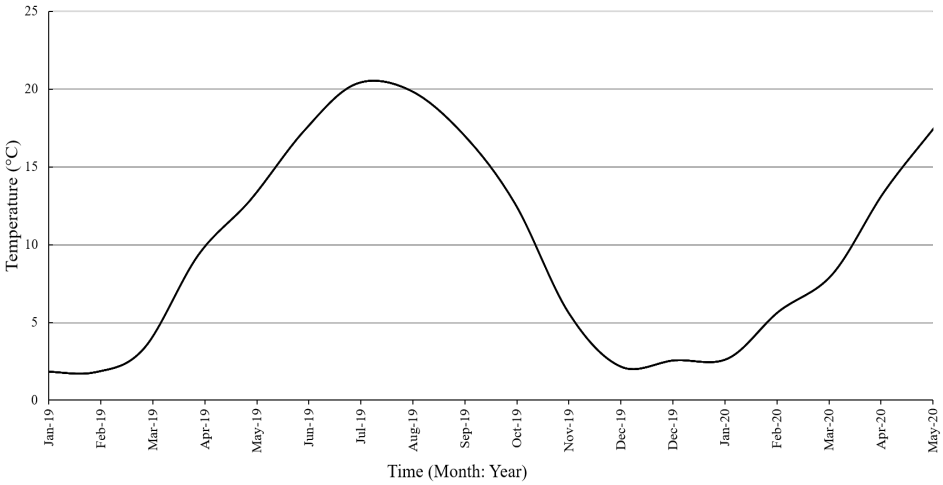

Figure A.2: Average water temperature by month

Table A.1: Water temperature data sets

ID	Link
1	https://waterdata.usgs.gov/ma/nwis/uv/?site_no=01104460&PARAmeter_cd=00065,00060
2	https://waterdata.usgs.gov/ma/nwis/uv/?site_no=01104420&PARAmeter_cd=00065,00060
3	https://waterdata.usgs.gov/ma/nwis/uv/?site_no=01104410&PARAmeter_cd=00065,00060
4	https://waterdata.usgs.gov/ma/nwis/uv/?site_no=01104370&PARAmeter_cd=00065,00060
5	https://waterdata.usgs.gov/ma/nwis/uv/?site_no=01104430&PARAmeter_cd=00065,00060
6	https://waterdata.usgs.gov/ma/nwis/uv/?site_no=01104455&PARAmeter_cd=00065,00060
7	https://waterdata.usgs.gov/ma/nwis/uv/?site_no=01104475&PARAmeter_cd=00065,00060
8	https://nwis.waterdata.usgs.gov/usa/nwis/uv/?cb_00010=on&format=gif_default&site_no=01095503&period=&begin_date=2020-07-01&end_date=2020-07-31
9	https://waterdata.usgs.gov/ma/nwis/uv/?site_no=01095220&PARAmeter_cd=00065,00060
10	https://waterdata.usgs.gov/ma/nwis/uv/?site_no=01095375&PARAmeter_cd=00065,00060
11	https://waterdata.usgs.gov/ma/nwis/uv/?site_no=01095434&PARAmeter_cd=00065,00060
12	https://waterdata.usgs.gov/ma/nwis/uv/?site_no=01095503&PARAmeter_cd=00065,00060
13	https://waterdata.usgs.gov/ma/nwis/uv/?site_no=01173000&PARAmeter_cd=00065,00060
14	https://waterdata.usgs.gov/ma/nwis/uv/?site_no=01170100&PARAmeter_cd=00065,00060
15	https://waterdata.usgs.gov/ma/nwis/uv/?site_no=01161280&PARAmeter_cd=00065,00060
16	https://waterdata.usgs.gov/ma/nwis/uv/?site_no=01104425&PARAmeter_cd=00062,72020,72022,62614
17	https://waterdata.usgs.gov/ma/nwis/uv/?site_no=01168250&PARAmeter_cd=00065,00060
18	https://waterdata.usgs.gov/ma/nwis/uv/?site_no=413601070275800&PARAmeter_cd=00065,00060

6.2 Appendix B: Procedure used for laboratory tests

1. GPR test.

2. Flash thermography with camera at 0, 15, and 30 degrees.
   a. Flash light to the roadway for <1 s and collect IR images with camera at 0 degrees
   b. Repeat procedure for other angles (making sure that the camera is always pointing at the same location on the roadway)

3. Passive thermography for 0, 15, and 30 degree settings.
   a. Uniform heating of road surface using two 1.5 kW lamps for ~6 h
   b. Thermography while surface cools down every 10 min
   c. Collect IR image with camera set at 0 degrees, then move to 15 degrees, and 30 degrees (making sure that the camera is pointing at the same location on the roadway)
   c. Wait 10 min from the time the first photo was taken and repeat the IR image acquisition for the three angles selected as described in 3c
   d. Repeat point 3b at 10-minute intervals for 1 h (a total of six data sets is recorded)

4. Effects of tires thermal signature.
   a. Warm up a heat pad in the microwave for 3 min at the maximum power
   b. Place the heat pad on the roadway always in the same position for 3 min
   c. Remove the heat pad from the road and record an IR image with camera set at 0 degrees, then move to 15 degrees, and 30 degrees

5. Effects of water on the data.
   a. Uniform heating of road surface using two 1.5 kW lamps for ~6 h
   b. Pour a known quantity of water on the surface of the roadway
   c. Thermography while surface cools down every 10 min
   d. Collect IR image with camera set at 0 degrees, then move to 15 degrees, and 30 degrees (making sure that the camera is pointing at the same location on the roadway)
   e. Wait 10 min from the time the first photo was taken and repeat the IR images acquisition for the three angles selected as described in 5d
   f. Collect IR image with camera set at 0 degrees, then move to 15 degrees, and 30 degrees

6. Remove a known volume of soil to increase the size of the defect.
   a. Measure the volume of soil removed

7. Repeat steps 1–6.

6.3 Appendix C: Procedure for outdoor validation tests

Day 1

1. Fly UAS on the edge of the road at location 1 at an altitude of 50 ft (15 m) and collect one IR image every 30 s for 8 min.

2. Fly UAS on the edge of the road at location 1 at an altitude of 60 ft (18 m) and collect one IR image every 30 s for 8 min.

3. Fly UAS on the edge of the road at location 1 at an altitude of 70 ft (21 m) and collect one IR image every 30 s for 8 min.

4. Move to location 2 and repeat steps 1–3.

5. Move to location 3 and repeat steps 1–3.

Day 2

Approach 1

6. Fly UAS on the edge of the road at location 1 at an altitude of 60 ft (18 m) and collect one IR image with camera in nadiral position.

7. Move to location 3.

8. Fly UAS on the edge of the road at location 3 at an altitude of 60 ft (18 m) and collect one IR image with camera in nadiral position.

9. Repeat steps 6 and 8 six times to collect IR images to perform PCT and S-PCT.

Approach 2

10. Fly UAS at location 3 at 60 ft (18 m) altitude by running preplanned flight to collect IR images and generate an orthomosaic (i.e., fly on the road from point A to point B).

11. Repeat step 10 six times with a 15-min time interval between subsequent flights.

Day 3

12. Fly UAS at night at location 3 at 60 ft (18 m) altitude by running preplanned flight to collect IR images and generate an orthomosaic (i.e., fly on the road from point A to point B).

13. Repeat step 12 six times with a 15-min time interval between subsequent flights.

6.4 Appendix D: Code for R^2-based analysis

```
import pandas as pd

T0 = pd.read_csv(r'C:\Users\Nitin_Kulkarni\Desktop\MASSDOT
TEST\D7_2\Temp\T01.csv')
T1 = pd.read_csv(r'C:\Users\Nitin_Kulkarni\Desktop\MASSDOT
TEST\D7_2\Temp\T11.csv')

NT0 = T0.to_numpy()
NT1 = T1.to_numpy()

def sum(x, chunk_size, axis=-1):
    shape = x.shape
    if axis < 0:
        axis += x.ndim
    shape = shape[:axis] + (-1, chunk_size) + shape[axis+1:]
    x = x.reshape(shape)
    return x.sum(axis=axis+1)

import numpy as np

NN0=sum(NT0,4)
N0T=np.transpose(NN0)
N0=sum(N0T,4)
N0=N0/16
N0=N0.flatten()

NN1=sum(NT1,4)
N1T=np.transpose(NN1)
N1=sum(N1T,4)
N1=N1/16
N1=N1.flatten()

Temp_decay= np.vstack((N0,N1))

import matplotlib.pyplot as plt
x=np.array([0,1,2,3,4,5,6,7,8,9,10,11])
for i in range(10):
    plt.plot( x , Temp_decay[ i , : ] )

plt.xlabel("Number of thermograms")
plt.ylabel("Temprature")
plt.savefig("temp decay.jpg", dpi=150)
plt.show()
```

```
z = np.std(Temp_decay,axis=1)
index=np.arange(20480)
z1=np.vstack((z,index)).T
sort = z1[np.argsort(z1[:, 0])]

xs = np.arange(12) + 7
ys=Temp_decay[ 5000 , : ]
plt.plot(xs, Temp_decay[ 4025 , : ] , '.')
plt.title("Original Data")

def monoExp(x, m, t, b):
    return m * np.exp(-t * x) + b

import scipy.optimize

p0 = (2000, .1, 50) # start with values near those we expect
params, cv = scipy.optimize.curve_fit(monoExp, xs, ys, p0)
m, t, b = params
sampleRate = 20_000 # Hz
tauSec = (1 / t) / sampleRate

# determine quality of the fit
squaredDiffs = np.square(ys - monoExp(xs, m, t, b))
squaredDiffsFromMean = np.square(ys - np.mean(ys))
rSquared = 1 - np.sum(squaredDiffs) / np.sum(squaredDiffsFromMean)
print(f"R² = {rSquared}")

# plot the results
plt.plot(xs, ys, '.', label="data")
plt.plot(xs, monoExp(xs, m, t, b), '--', label="fitted")
plt.xlabel("Time")
plt.ylabel("Temprature")
plt.savefig("Defect fit.jpg", dpi=150)
plt.show()
# inspect the parameters
print(f"Y = {m} * e^(-{t} * x) + {b}")

length = len(Temp_decay)
a = np.zeros((length),dtype=float)
for i in range(length):
    xs = np.arange(12) + 7
    ys=Temp_decay[ i , : ]
    params, cv = scipy.optimize.curve_fit(monoExp, xs, ys, p0)
    m, t, b = params
    squaredDiffs = np.square(ys - monoExp(xs, m, t, b))
    squaredDiffsFromMean = np.square(ys - np.mean(ys))
```

```
    a[i] = 1 - np.sum(squaredDiffs) / np.sum(squaredDiffsFromMean)

R2 = np.reshape(a, (160,128))
R2=np.transpose(R2)

color_map=plt.imshow(R2)
color_map.set_cmap('gist_rainbow')
plt.colorbar()

plt.xlabel("Pixels")
plt.ylabel("Pixel")
plt.savefig("Defect.jpg", dpi=150)
plt.show()
```

6.5 Appendix E: Code for PCT- and S-PCT-based analysis

```
import pandas as pd
import matplotlib.pyplot as plt
import numpy as np
import seaborn as sns

T0 = pd.read_csv(r'C:\Users\Nitin_Kulkarni\Desktop\MassDOT Outdoor test\Location
3\Excelq\T01.csv')
T1 = pd.read_csv(r'C:\Users\Nitin_Kulkarni\Desktop\MassDOT Outdoor test\Location
3\Excelq\T11.csv')

N0 = T0.to_numpy()
N1 = T1.to_numpy()

import numpy as np

N0=N0.flatten()
N1=N1.flatten()

N= np.vstack((N0,N1)).T

from sklearn import preprocessing
standard = preprocessing.scale(N)
print(standard)
projection_matrix = (eigen_vectors.T[:1]).T
print(projection_matrix)

np.fill_diagonal(T,eigen_values)
V = eigen_vectors
V=np.transpose(V)

V1=np.linalg.inv(V)
T1=np.linalg.inv(T)

U=N.dot(V1).dot(T1)

U1=np.transpose(U)


EOF1 = np.reshape(U1[0,:], (512,640))
EOF2 = np.reshape(U1[1,:], (512,640))


color_map=plt.imshow(EOF2)
color_map.set_cmap("gist_rainbow")
```

```
plt.colorbar()

plt.xlabel("Pixels")
plt.ylabel("Pixel")
plt.savefig("Defect.jpg", dpi=150)
plt.show()

from sklearn.decomposition import SparsePCA
from numpy import reshape
import seaborn as sns
import pandas as pd

spca = SparsePCA(n_components=2, random_state=123)
z=spca.fit_transform(N)

z=np.transpose(z)
EOF11 = np.reshape(z[0,:], (512,640))
EOF22 = np.reshape(z[1,:], (512,640))

z=np.transpose(z)
EOF11 = np.reshape(z[0,:], (512,640))
EOF22 = np.reshape(z[1,:], (512,640))
```